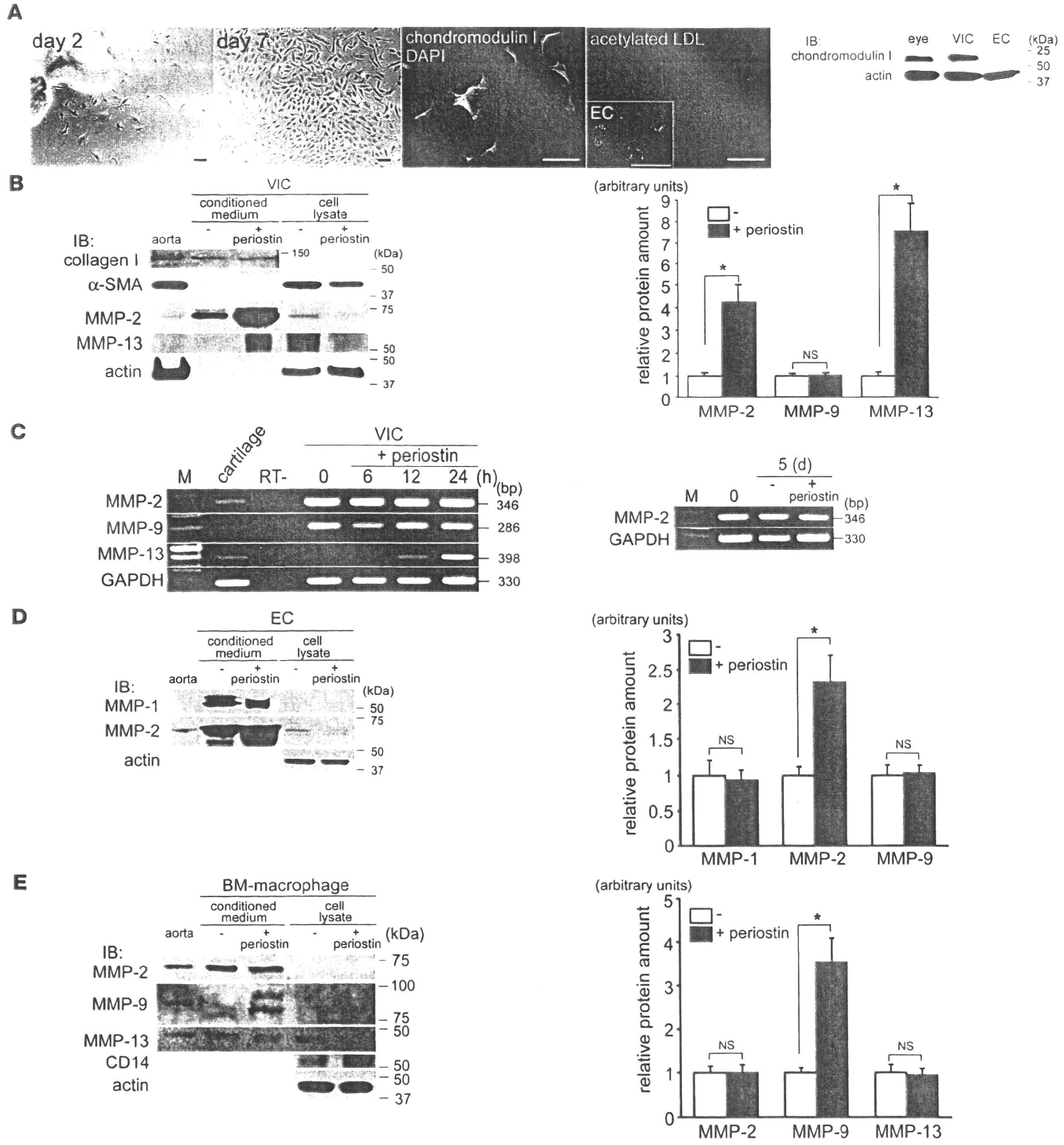

Figure 8

Periostin induces the secretion of MMPs from VICs, ECs, and macrophages in vitro. (**A**) Light microscopy, immunofluorescence staining, and Western blot analysis of cultured rat VICs. The VICs were fibroblast-like in appearance and expressed chondromodulin I, but did not express acetylated LDL. The ECs in the inset and the rat eye in the Western blot served as positive controls. Scale bars: 100 μm. (**B**) Expression and secretion of collagen I, α-SMA, MMP-2, and MMP-13 by VICs following periostin stimulation. Conditioned media and cell lysates were obtained from VICs with or without periostin stimulation and subjected to Western blot analysis. Periostin prominently stimulated secretion of MMP-2 and MMP-13 by VICs, whereas collagen I production and α-SMA expression were unchanged. Densitometric quantitative analysis of MMP levels in the conditioned media from the VIC cultures is also shown. (**C**) RT-PCR analysis of MMP expression in VICs after periostin stimulation. Periostin increased the transcription of *Mmp13*, but not that of *Mmp2* or *Mmp9*. Cartilage served as a positive control. Also shown is *Mmp2* mRNA expression in VICs after stimulation with or without periostin for 5 days. (**D** and **E**) Expression and secretion of MMPs by human coronary artery ECs (**D**) and cultured mouse BM-derived macrophages (**E**) following periostin stimulation. Densitometric quantitative analyses of MMP levels in the conditioned media from cultures of ECs and macrophages is also shown. Periostin significantly induced secretion of MMP-2 and MMP-9 from ECs and macrophages, respectively. $^*P < 0.05$.

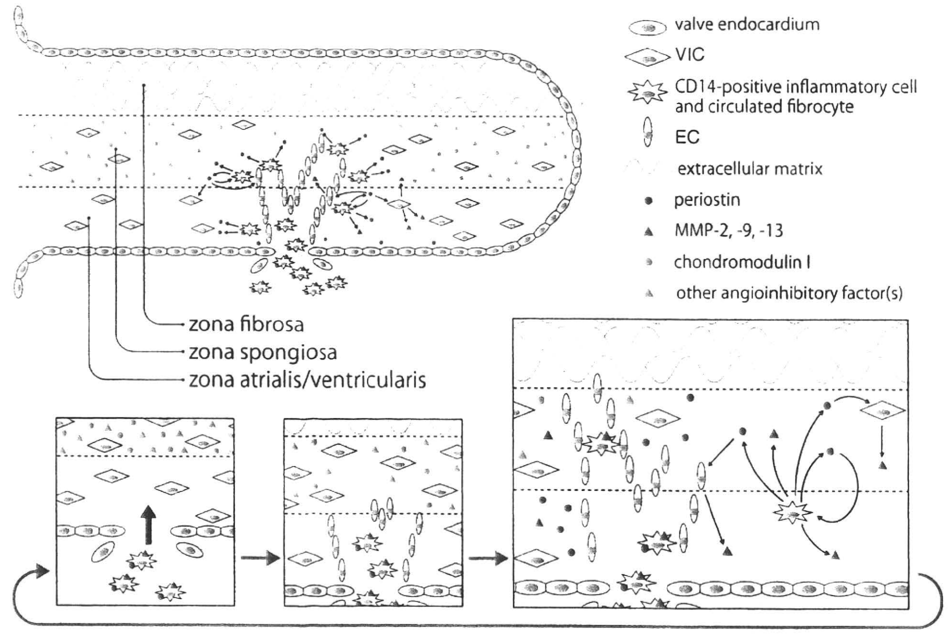

Figure 9

Conceptual framework for the roles of periostin and chondromodulin I in the progression of atherosclerotic and rheumatic VHD. The circulating CD14-positive inflammatory cells (and possibly fibrocytes) that express periostin initially infiltrate the zona atrialis/ventricularis of the cardiac valve. Thereafter, periostin secreted from these cells not only promotes angiogenesis by induction of EC migration and inhibition of EC apoptosis, but also stimulates the production of MMP-2, MMP-9, and MMP-13 by ECs, VICs, and engrafted macrophages, which advance cardiac valve degeneration. Valve degeneration in turn facilitates the infiltration of circulating periostin-expressing cells, thereby creating a vicious circle. The origin of the engrafted ECs is unknown; it is possible that periostin enhances the recruitment of circulating endothelial progenitor cells into the valves or promotes the penetration of microvessels from the annulus region or roots into the leaflets. In contrast, chondromodulin I blocks angiogenesis through inhibition of EC migration and induction of EC apoptosis, although other angioinhibitory factors are involved during the earlier stages of valve degeneration. Therefore, the equilibrium between periostin and chondromodulin I (as well as other angioinhibitory factors) defines the progression of atherosclerotic and rheumatic cardiac valve degeneration by controlling angiogenesis and MMP production.

expressing exogenous inflammatory cells and myofibroblasts, thereby creating a vicious circle in degenerative VHD (Figure 9).

The HF diet significantly induced the expression of periostin, α-SMA, MMP-2, and MMP-13 in the cardiac valve complexes of WT mice, although the underlying mechanism remains unclear. Because the periostin promoter contains a site for activator protein-1 (AP-1) and a Smad binding element (63) and is induced by various cellular stresses (64), we hypothesize that the upregulation of periostin expression is due to periostin induction and/or the accumulation of exogenous myofibroblasts and inflammatory cells as a result of HF diet–provoked oxidative stress and inflammation.

The HF diet increased body weights and serum total cholesterol levels by 1.8-fold in both WT and *Postn*$^{-/-}$ mice, reflecting the increases observed clinically in humans. Surprisingly, degeneration and the expression of α-SMA, MMP-2, and MMP-13 in the cardiac valve complex were strikingly diminished in the *Postn*$^{-/-}$ mice. The detailed mechanisms underlying this phenotypic change are not elucidated by this experiment, given the limitation that the role of periostin in specific cell types is not demonstrable in the germline knockout mice used. However, it is possible that these findings reflect the decreased abilities of myofibroblasts and inflammatory cells to adhere to and infiltrate the valves of *Postn*$^{-/-}$ mice. In support of this notion, a recent study showed that the number of α-SMA–positive cells was significantly lower in the infarct areas of *Postn*$^{-/-}$ mice than in those of WT mice and that adenovirus-mediated *Postn* gene transfer into the knockout mice restored the number of α-SMA–positive cells to the levels seen in WT mice (37).

In the present study, we focused on the pathophysiologic functions of periostin in degenerative atherosclerotic and rheumatic VHD and found that periostin is a critical factor in the degeneration of the cardiac valve complex. The therapeutic effect of HMG CoA reductase inhibitors on aortic valve stenosis is currently a controversial issue. Therefore, periostin may represent a novel therapeutic target to prevent the progression of atherosclerotic and rheumatic VHD, including aortic valve stenosis. Further studies are required to address this issue.

Methods

Animals. WT ICR mice and Wistar rats were purchased from Japan CLEA. The genetic backgrounds of the *Postn*$^{-/-}$ mice (37) and the *Lect1*$^{-/-}$ mice (23) have been described previously. The offspring were genotyped by either Southern blotting or PCR, and WT littermates of these knockout strains were used as controls. All experimental procedures and protocols were approved by the Animal Care and Use Committee of Keio University and conformed to NIH guidelines for the care and use of laboratory animals.

Human samples. Samples of 10 aortic and 11 mitral valves were collected from patients (9 males and 12 females; average age, 63.9 ± 12.0 years) who were undergoing valve replacement surgery due to valvular stenosis or regurgitation. The average ages of the patients with atherosclerotic valves ($n = 8$), rheumatic valves ($n = 9$), and valvular prolapse ($n = 4$) were 70.0 ± 9.2 years, 64.7 ± 7.8 years, and 50.0 ± 15.3 years, respectively. Specimens were fixed in formaldehyde immediately after removal and then embedded in paraffin. As controls, 12 microscopically and macroscopically normal, noncalcified, smooth, and pliable valves (7 aortic and 5 mitral valves) were collected from 10 autopsied patients (8 males and 2 females; average age, 65.2 ± 5.8 years) who died of noncardiac diseases. The use of autopsied and surgical specimens of human tissues was approved by the institutional review board of Keio University. All participants provided informed consent for their tissue to be used.

RT-PCR. Total RNA was prepared with the TRIzol reagent (Gibco; Invitrogen). RT-PCR was performed as described previously (23) using the following primers: mouse *Postn* forward, 5′-AACCAAGGACCTGAAACACG-3′; mouse *Postn* reverse, 5′-CAAAGAGCGTGAAGTGACCA-3′; mouse *Postn* primer pair 1 forward, 5′-GATAAAATACATCCAAATCAAGTTTGTTCG-3′; mouse *Postn* primer pair 1 reverse, 5′-AAACTCTGTGGTCTGGCCTCTGGG-3′; mouse *Postn* primer pair 2 forward, 5′-GATAAAATA-

CATCCAAATCAAGTTTGTTCG-3′; mouse *Postn* primer pair 2 reverse, 5′-CGTGGATCACTTCTGTCACCGTTTCGC-3′; mouse *Lect1* forward 1, 5′-TTGGTTGATGCTTCAGTGTG-3′; mouse *Lect1* forward 2, 5′-CCGCTTCCTCGTGCTTTACGG-3′; mouse *Lect1* reverse, 5′-CTTGTGCACAGACCAGAACAA-3′; mouse *GAPDH* forward, 5′-TTCAACGGCACAGTCAAGG-3′; mouse *GAPDH* reverse, 5′-CATGGACTGTGGTCATGAG-3′; rat *Mmp2* forward, 5′-ACACTGGGACCTGTCACTCC-3′; rat *Mmp2* reverse, 5′-TCCAGTTAAAGGCAGCGTCT-3′; rat *Mmp9* forward, 5′-CACTGTAACTGGGGGCAACT-3′; rat *Mmp9* reverse, 5′-AGGGGAGTCCTCGTGGTAGT-3′; rat *Mmp13* forward, 5′-TGTGGCTGGCTTTACATTTG-3′; rat *Mmp13* reverse, 5′-ACATGGAGGAGCATGAAAGG-3′; rat *Lect1* forward, 5′-AAGCAGTGCTCCCTCTACCA-3′; rat *Lect1* reverse, 5′-AATTCTTGCTTGGCAGTGCT-3′.

Western blotting. Western blot analysis was performed as described previously (23). To obtain cell lysates, murine cardiac valves were homogenized, then concentrated using a Microcon centrifugal ultrafiltration filter (Millipore). The primary antibodies used were as follows: anti-mouse periostin antibody (directed against the C-terminus of periostin and recognizing both the long and short isoforms; ref. 37); anti-periostin (provided by R. Markwald, Medical University of South Carolina, Charleston, South Carolina, USA); anti-α-SMA (Sigma-Aldrich); anti-collagen type I (C-18; Santa Cruz Biotechnology); anti-phospho-FAK (Tyr397; Cell Signaling Technology); anti-FAK (Cell Signaling Technology); anti-phospho-Akt (Ser473; Cell Signaling Technology); anti-Akt (Cell Signaling Technology); anti-MMP-1 (SA-102; BIOMOL Research Laboratories); anti-MMP-2 (42-5D11; Daiichi Fine Chemical); anti-MMP-9 (C-20; Santa Cruz Biotechnology); and anti-MMP-13 (AB8120; Chemicon International). The level of total protein was assessed by reblotting with anti-actin antibody (C-11; Santa Cruz Biotechnology) or by staining with Ponceau-S (Sigma-Aldrich).

Histology, immunohistochemistry, and immunofluorescence staining. Mouse and rat specimens were perfused from the apex with 4% paraformaldehyde, fixed overnight, and then embedded in paraffin; histology and immunostaining were performed as previously described (23). Some samples were embedded in OCT compound (Sakura Finetek Japan) after fixation, and then frozen in liquid nitrogen. Primary antibodies were as follows: anti-periostin (provided by R. Markwald; for triple immunofluorescence, MAB3548; R&D Systems); anti-periostin antibody 1 (RD181045050; BioVendor); anti-periostin antibody 2 (directed against the N-terminus of human periostin); anti-chondromodulin I (23); anti-vWF (A0 and R7; Thermo Scientific); anti-VEGF (A-20; Santa Cruz Biotechnology); anti-collagen type I (Rockland); anti-elastin (Elastin Products); anti-vimentin (GP53; PROGEN Biotechnik); anti-CD14 (M-305; Santa Cruz Biotechnology); anti-cadherin 11 (5B2H5; Invitrogen); and anti-NFATc1 (7A6; BD Biosciences – Pharmingen). The M.O.M. Immunodetection Kit (Vector Laboratories) was used to detect the mouse primary antibody used to blot the murine tissues.

For IHC, antigen unmasking was performed by heating in a microwave oven the sections in 10 mM citric acid monohydrate (pH 6.0; DAKO) for 3 minutes. Immunohistochemical signals were then detected using the DakoCytomation EnVision+ System-HRP (DAB) Kit (DAKO) or the Universal LSAB+ Kit/HRP for Mouse/Rabbit/Goat (DAKO). Percentages of stained areas in the sections were analyzed using NIH Image J software version 1.37.

For immunofluorescence analyses, sections were incubated with secondary antibodies conjugated with Alexa Fluor 488 or Alexa Fluor 546 (Invitrogen). The slides were observed under a confocal laser-scanning microscope (LSM 510 META; Carl Zeiss) or an immunofluorescence microscope (BIOREVO BZ-9000; Keyence). As a negative control in each immunostaining experiment, nonimmune rabbit serum was substituted for the primary antibody.

Feeding protocol. *Postn*$^{-/-}$ mice and their WT littermates at 12 weeks of age were fed either normal diet CE-2 (Japan CLEA) or High Fat Diet 32 (Japan CLEA) for 4 months, and were then subjected to analysis. In the HF diet, 57% of the total calories are derived from fat, compared with 10% in the normal diet.

Echocardiography. Transthoracic echocardiography was performed on WT and *Postn*$^{-/-}$ mice ($n = 8$ per group) using a Vevo 770 echocardiogram (VisualSonics) equipped with a 45-MHz sector-array transducer. Mice were anesthetized with isoflurane inhalation, and the hearts were scanned at a rate of 100 frames/s using 2D mode or M-mode. The high-echogenic areas of the aortic and mitral valve annuli were traced using the 2D mode of the long axis view. The aortic valve thickness, the thickness of the interventricular septum and LV posterior wall, and the end-diastolic and end-systolic diameters of the LV were measured using the M-mode of the long axis view.

Preparation of adenovirus. Construction of adenoviruses that express either the long or the short isoform of mouse periostin or nuclear localization signal-LacZ was performed with the Adeno-X Expression System 2 (BD Biosciences), as described previously (37). COS7 cells were infected with these adenoviruses in serum-free DMEM, and the conditioned media were collected.

Isolation and primary culture of adult rat VICs and mouse BM-derived macrophages. The isolation and primary culture of VICs were performed according to the previously described protocol (23), with minor modifications. The valvular pieces cut by a blade were grown in M199 medium (Sigma-Aldrich) with 50% FBS for 24 hours at 37°C. Medium was then replaced with M199 that contained 10% FBS.

Mouse BM-derived macrophages were isolated as previously described (65). Briefly, the femur and tibia were excised from the mice, cut at both ends, and flushed with the medium using a syringe. The BM cells were plated and cultured for 7 days at a concentration of 2×10^6 cells/ml in RPMI 1640 GlutaMAX I medium (Invitrogen) supplemented with 10% FBS, 1% penicillin-streptomycin, and 50 μg/ml recombinant human M-CSF (PeproTech). Cells were washed with PBS, and the medium was changed every 3 days. More than 95% of the cells were identified as macrophages based on nonspecific esterase staining.

Cell culture. Human coronary artery ECs were purchased from Takara Biotechnology, maintained as described previously (23), and used at passages 3–5. MC3T3-E1 cells (ATCC) were purchased and maintained according to the manufacturer's instructions. In some experiments, VICs and ECs were treated with 10 μg/ml DiI-conjugated acetylated LDL (Invitrogen) for 1 hour at 37°C and observed under an immunofluorescence microscope. For the MMP production analyses, VICs, coronary artery ECs, and BM-derived macrophages were serum-starved and stimulated for 7 days (VICs) or 2 days (ECs and macrophages) with 5 μg/ml recombinant human periostin (R&D Systems), which corresponds to the long isoform of periostin, and the conditioned media and cell lysates were collected. In some experiments, BM-derived macrophages were stimulated with or without 50 μM H_2O_2 (Wako), 10 ng/ml recombinant human TNF-α (R&D Systems), 10 μg/ml LPS (from *E. coli* 0111:B4; Sigma-Aldrich), or 10 ng/ml human TGF-β_1 (R&D Systems) for 24 hours.

Tube formation assay. A tube formation assay using ECs was performed as described previously (23), with minor modifications. After incubation for 4 hours under starvation conditions, the ECs were trypsinized and suspended in conditioned medium, which contained the long or short periostin isoform or LacZ. The assays were performed with 6 replicates.

Cell migration assay. The cell migration assay was performed as described previously (23), with minor modifications. ECs were cultured in modified Boyden chambers with 8-μm-pore filter inserts (Chemotaxicell; Kurabo) for 24-well plates (BD Labware). The conditioned medium was placed in the lower chamber, and ECs were seeded (5×10^4 cells per well) into the upper chamber under serum-free conditions. The assays were performed with 6 replicates.

In vitro 3D vasculogenesis assay. The 3D vasculogenesis assay for ECs was performed according to a previously described protocol (66), with minor modifications. Rat tail collagen (High Concentration, type 1; BD Biosciences), 1 N NaOH, and serum-free EBM-2 (Lonza) with or without periostin were mixed on ice to prepare the collagen I solution. The ECs were trypsinized and added to the collagen solution to produce the EC-collagen mixture (1×10^6 cells/ml and 3 mg/ml collagen). Aliquots (50 μl) of the mixture were placed in the wells of a 96-well plate and allowed to gel at 37°C for 30 minutes. EBM-2 supplemented with 0.5 mg/ml BSA and 1% ITS Liquid Media Supplement (Sigma-Aldrich) was added to each well and incubated at 37°C for 24 hours. The cells were fixed with 2% PFA overnight, stained with 0.05% toluidine blue solution (Muto Pure Chemicals) for 45 minutes, washed with water for 2 hours, and observed under a phase-contrast microscope. The assays were performed with 6 replicates.

Cell proliferation assay. The effects of periostin on EC and VIC proliferation were examined using the BrdU Labeling and Detection Kit I (Roche Diagnostics) according to the manufacturer's instructions. Cells were grown to 50% confluence, and then starved for 4 hours (ECs) or 24 hours (VICs). The cells were then incubated with 10 μM BrdU for 2 hours and subjected to immunostaining. The fluorescent cells in 4 random fields per well were counted under an immunofluorescence microscope. The assays were performed with 5 replicates.

Apoptosis assay. The annexin V-FITC Apoptosis Detection Kit (BioVision) was used according to the manufacturer's instructions. ECs or VICs were cultured in medium with or without periostin. The cells were then labeled with annexin V-FITC and propidium iodide, washed with PBS, and fixed with 2% formaldehyde for 15 minutes. The annexin V-positive, propidium iodide-negative cells in 4 random fields per well were counted under an immunofluorescence microscope. The assays were performed with 6 replicates.

Ex vivo aortic ring angiogenesis assay. The aortic ring assay was performed as previously described (65). Briefly, the aortic roots and annuli just above the aortic valves were dissected from WT and *Postn*$^{-/-}$ mice, cleaned of blood and periaortic fibroadipose tissue, and sectioned into 1-mm rings with a scalpel. The aortic root rings were embedded in 2 mg/ml collagen I gel so that the luminal axis lay parallel to the bottom of the well. The rings were cultured in serum-free EBM-2 in 96-well plates at 37°C, and the medium was replaced every 3 days. The microvessels that radiated outward from the aortic root were counted at the indicated time points under a phase-contrast microscope. In some experiments, 5 μg/ml recombinant human periostin was added to the medium. The assays were performed with 6 replicates.

Statistics. All results are presented as mean ± SD. Statistical significance was evaluated with the unpaired 2-tailed Student's *t* test for comparisons between 2 mean values. Multiple comparisons of more than 3 groups were performed by ANOVA. *P* values of less than 0.05 were considered statistically significant.

Acknowledgments

We thank Yoshiko Miyake for expert technical assistance with the histology. This study received support from the program for the Promotion of Fundamental Studies in Health Science of the National Institute of Biomedical Innovation (NIBIO; to K. Fukuda), Grants-in-Aid for Scientific Research from the Ministry of Education, Culture, Sports, Science, and Technology of Japan (to D. Hakuno and K. Fukuda), a Japan Heart Foundation/Novartis Grant for Research Award on Molecular and Cellular Cardiology (to D. Hakuno), and a grant from the Keio Gijuku Fund for the Advancement of Education and Research (to D. Hakuno).

Received for publication August 27, 2009, and accepted in revised form April 21, 2010.

Address correspondence to: Keiichi Fukuda, Department of Regenerative Medicine and Advanced Cardiac Therapeutics, Keio University School of Medicine, 35 Shinanomachi, Shinjuku-ku, Tokyo 160-8582, Japan. Phone: 81.3.5363.3874; Fax: 81.3.5363.3875; E-mail: kfukuda@sc.itc.keio.ac.jp.

Daihiko Hakuno's present address is: Cardiovascular Division, Department of Internal Medicine, National Defense Medical College, Saitama, Japan.

1. Nkomo VT, Gardin JM, Skelton TN, Gottdiener JS, Scott CG, Enriquez-Sarano M. Burden of valvular heart diseases: a population-based study. *Lancet.* 2006;368(9540):1005–1011.
2. Mohler ER 3rd, Gannon F, Reynolds C, Zimmerman R, Keane MG, Kaplan FS. Bone formation and inflammation in cardiac valves. *Circulation.* 2001;103(11):1522–1528.
3. Freeman RV, Otto CM. Spectrum of calcific aortic valve disease: pathogenesis, disease progression, and treatment strategies. *Circulation.* 2005;111(24):3316–3326.
4. Aikawa E, et al. Multimodality molecular imaging identifies proteolytic and osteogenic activities in early aortic valve disease. *Circulation.* 2007;115(3):377–386.
5. Rajamannan NM, Bonow RO, Rahimtoola SH. Calcific aortic stenosis: an update. *Nat Clin Pract Cardiovasc Med.* 2007;4(5):254–262.
6. Cowell SJ, et al. A randomized trial of intensive lipid-lowering therapy in calcific aortic stenosis. *N Engl J Med.* 2005;352(23):2389–2397.
7. Rossebo AB, et al. Intensive lipid lowering with simvastatin and ezetimibe in aortic stenosis. *N Engl J Med.* 2008;359(13):1343–1356.
8. Satta J, et al. Progression of human aortic valve stenosis is associated with tenascin-C expression. *J Am Coll Cardiol.* 2002;39(1):96–101.
9. Caira FC, et al. Human degenerative valve disease is associated with up-regulation of low-density lipoprotein receptor-related protein 5 receptor-mediated bone formation. *J Am Coll Cardiol.* 2006;47(8):1707–1712.
10. Walker GA, Masters KS, Shah DN, Anseth KS, Leinwand LA. Valvular myofibroblast activation by transforming growth factor-beta: implications for pathological extracellular matrix remodeling in heart valve disease. *Circ Res.* 2004;95(3):253–260.
11. Kaden JJ, et al. Receptor activator of nuclear factor kappaB ligand and osteoprotegerin regulate aortic valve calcification. *J Mol Cell Cardiol.* 2004;36(1):57–66.
12. Osman L, et al. A novel role of the sympatho-adrenergic system in regulating valve calcification. *Circulation.* 2007;116(11 suppl):I282–I287.
13. Hakuno D, Kimura N, Yoshioka M, Fukuda K. Molecular mechanisms underlying the onset of degenerative aortic valve disease. *J Mol Med.* 2009;87(1):17–24.
14. Galvin KM, et al. A role for smad6 in development and homeostasis of the cardiovascular system. *Nat Genet.* 2000;24(2):171–174.
15. Hanada K, et al. Perturbations of vascular homeostasis and aortic valve abnormalities in fibulin-4 deficient mice. *Circ Res.* 2007;100(5):738–746.
16. Garg V, et al. Mutations in NOTCH1 cause aortic valve disease. *Nature.* 2005;437(7056):270–274.
17. Hammon JW Jr, O'Sullivan MJ, Oury J, Fosburg RG. Allograft cardiac valves. A view through the scanning electron microscope. *J Thorac Cardiovasc Surg.* 1974;68(3):352–360.
18. Millington-Sanders C, Meir A, Lawrence L, Stolinski C. Structure of chordae tendineae in the left ventricle of the human heart. *J Anat.* 1998;192(pt 4):573–581.
19. Shukunami C, Oshima Y, Hiraki Y. Chondromodulin-I and tenomodulin: a new class of tissue-specific angiogenesis inhibitors found in hypovascular connective tissues. *Biochem Biophys Res Commun.* 2005;333(2):299–307.
20. Ashraf S, Walsh DA. Angiogenesis in osteoarthritis. *Curr Opin Rheumatol.* 2008;20(5):573–580.
21. Soini Y, Salo T, Satta J. Angiogenesis is involved in the pathogenesis of nonrheumatic aortic valve stenosis. *Hum Pathol.* 2003;34(8):756–763.
22. Rajamannan NM, et al. Calcified rheumatic valve neoangiogenesis is associated with vascular endothelial growth factor expression and osteoblast-like bone formation. *Circulation.* 2005;111(24):3296–3301.
23. Yoshioka M, et al. Chondromodulin-I maintains cardiac valvular function by preventing angiogenesis. *Nat Med.* 2006;12(10):1151–1159.
24. Kimura N, et al. Local tenomodulin absence, angiogenesis, and matrix metalloproteinase activation are associated with the rupture of the chordae tendineae cordis. *Circulation.* 2008;118(17):1737–1747.
25. Takeshita S, Kikuno R, Tezuka K, Amann E. Osteoblast-specific factor 2: cloning of a putative bone adhesion protein with homology with the insect protein fasciclin I. *Biochem J.* 1993;294(pt 1):271–278.
26. Horiuchi K, et al. Identification and characterization of a novel protein, periostin, with restricted expression to periosteum and periodontal ligament and increased expression by transforming growth factor beta. *J Bone Miner Res.* 1999;14(7):1239–1249.
27. Zinn K, McAllister L, Goodman CS. Sequence analysis and neuronal expression of fasciclin I in grasshopper and Drosophila. *Cell.* 1988;53(4):577–587.

28. Gillan L, Matei D, Fishman DA, Gerbin CS, Karlan BY, Chang DD. Periostin secreted by epithelial ovarian carcinoma is a ligand for alpha(V)beta(3) and alpha(V)beta(5) integrins and promotes cell motility. *Cancer Res.* 2002;62(18):5358-5364.
29. Bao S, et al. Periostin potently promotes metastatic growth of colon cancer by augmenting cell survival via the Akt/PKB pathway. *Cancer Cell.* 2004;5(4):329-339.
30. Lindner V, Wang Q, Conley BA, Friesel RE, Vary CP. Vascular injury induces expression of periostin: implications for vascular cell differentiation and migration. *Arterioscler Thromb Vasc Biol.* 2005;25(1):77-83.
31. Roy S, et al. Transcriptome-wide analysis of blood vessels laser captured from human skin and chronic wound-edge tissue. *Proc Natl Acad Sci U S A.* 2007;104(36):14472-14477.
32. Kruzynska-Frejtag A, Machnicki M, Rogers R, Markwald RR, Conway SJ. Periostin (an osteoblast-specific factor) is expressed within the embryonic mouse heart during valve formation. *Mech Dev.* 2001;103(1-2):183-188.
33. Katsuragi N, et al. Periostin as a novel factor responsible for ventricular dilation. *Circulation.* 2004;110(13):1806-1813.
34. Oka T, et al. Genetic manipulation of periostin expression reveals a role in cardiac hypertrophy and ventricular remodeling. *Circ Res.* 2007;101(3):313-321.
35. Lorts A, Schwanekamp JA, Elrod JW, Sargent MA, Molkentin JD. Genetic manipulation of periostin expression in the heart does not affect myocyte content, cell cycle activity, or cardiac repair. *Circ Res.* 2009;104(1):e1-e7.
36. Stanton LW, et al. Altered patterns of gene expression in response to myocardial infarction. *Circ Res.* 2000;86(9):939-945.
37. Shimazaki M, et al. Periostin is essential for cardiac healing after acute myocardial infarction. *J Exp Med.* 2008;205(2):295-303.
38. Butcher JT, Norris RA, Hoffman S, Mjaatvedt CH, Markwald RR. Periostin promotes atrioventricular mesenchyme matrix invasion and remodeling mediated by integrin signaling through Rho/PI 3-kinase. *Dev Biol.* 2007;302(1):256-266.
39. Snider P, et al. Periostin is required for maturation and extracellular matrix stabilization of noncardiomyocyte lineages of the heart. *Circ Res.* 2008;102(7):752-760.
40. Lincoln J, Lange AW, Yutzey KE. Hearts and bones: shared regulatory mechanisms in heart valve, cartilage, tendon, and bone development. *Dev Biol.* 2006;294(2):292-302.
41. Getz GS, Reardon CA. Diet and murine atherosclerosis. *Arterioscler Thromb Vasc Biol.* 2006;26(2):242-249.
42. Drolet MC, Roussel E, Deshaies Y, Couet J, Arsenault M. A high fat/high carbohydrate diet induces aortic valve disease in C57BL/6J mice. *J Am Coll Cardiol.* 2006;47(4):850-855.
43. Visse R, Nagase H. Matrix metalloproteinases and tissue inhibitors of metalloproteinases: structure, function, and biochemistry. *Circ Res.* 2003;92(8):827-839.
44. Lindsey ML, et al. Selective matrix metalloproteinase inhibition reduces left ventricular remodeling but does not inhibit angiogenesis after myocardial infarction. *Circulation.* 2002;105(6):753-758.
45. Soini Y, Satta J, Maatta M, Autio-Harmainen H. Expression of MMP-2, MMP9, MT1-MMP, TIMP1, and TIMP2 mRNA in valvular lesions of the heart. *J Pathol.* 2001;194(2):225-231.
46. Jian B, Jones PL, Li Q, Mohler ER 3rd, Schoen FJ, Levy RJ. Matrix metalloproteinase-2 is associated with tenascin-C in calcific aortic stenosis. *Am J Pathol.* 2001;159(1):321-327.
47. Rabkin E, Aikawa M, Stone JR, Fukumoto Y, Libby P, Schoen FJ. Activated interstitial myofibroblasts express catabolic enzymes and mediate matrix remodeling in myxomatous heart valves. *Circulation.* 2001;104(21):2525-2532.
48. Butcher JT, et al. Transcriptional profiles of valvular and vascular endothelial cells reveal phenotypic differences: influence of shear stress. *Arterioscler Thromb Vasc Biol.* 2006;26(1):69-77.
49. Misfeldt AM, Boyle SC, Tompkins KL, Bautch VL, Labosky PA, Baldwin HS. Endocardial cells are a distinct endothelial lineage derived from Flk1+ multipotent cardiovascular progenitors. *Dev Biol.* 2009;333(1):78-89.
50. Shao R, et al. Acquired expression of periostin by human breast cancers promotes tumor angiogenesis through up-regulation of vascular endothelial growth factor receptor 2 expression. *Mol Cell Biol.* 2004;24(9):3992-4003.
51. Visconti RP, et al. An in vivo analysis of hematopoietic stem cell potential: hematopoietic origin of cardiac valve interstitial cells. *Circ Res.* 2006;98(5):690-696.
52. Bucala R. Fibrocytes: Discovery of a Circulating Connective Tissue Cell Progenitor. In: Bucala R, ed. *Fibrocytes: New Insights into Tissue Repair and Systemic Fibroses.* Toh Tuck Link, Singapore: World Scientific Publishing Company; 2007:1-18.
53. Ferrara N, Davis-Smyth T. The biology of vascular endothelial growth factor. *Endocr Rev.* 1997;18(1):4-25.
54. Siriwardena BS, et al. Periostin is frequently overexpressed and enhances invasion and angiogenesis in oral cancer. *Br J Cancer.* 2006;95(10):1396-1403.
55. Li YY, McTiernan CF, Feldman AM. Interplay of matrix metalloproteinases, tissue inhibitors of metalloproteinases and their regulators in cardiac matrix remodeling. *Cardiovasc Res.* 2000;46(2):214-224.
56. Oh J, et al. The membrane-anchored MMP inhibitor RECK is a key regulator of extracellular matrix integrity and angiogenesis. *Cell.* 2001;107(6):789-800.
57. Munesue S, et al. A novel function of syndecan-2, suppression of matrix metalloproteinase-2 activation, which causes suppression of metastasis. *J Biol Chem.* 2007;282(38):28164-28174.
58. Kleiner DE Jr, Tuuttila A, Tryggvason K, Stetler-Stevenson WG. Stability analysis of latent and active 72-kDa type IV collagenase: the role of tissue inhibitor of metalloproteinases-2 (TIMP-2). *Biochemistry.* 1993;32(6):1583-1592.
59. Mitchell PG, et al. Cloning, expression, and type II collagenolytic activity of matrix metalloproteinase-13 from human osteoarthritic cartilage. *J Clin Invest.* 1996;97(3):761-768.
60. Neuhold LA, et al. Postnatal expression in hyaline cartilage of constitutively active human collagenase-3 (MMP-13) induces osteoarthritis in mice. *J Clin Invest.* 2001;107(1):35-44.
61. Norris RA, et al. Periostin regulates collagen fibrillogenesis and the biomechanical properties of connective tissues. *J Cell Biochem.* 2007;101(3):695-711.
62. Jung JC, Wang PX, Zhang G, Ezura Y, Fini ME, Birk DE. Collagen fibril growth during chicken tendon development: matrix metalloproteinase-2 and its activation. *Cell Tissue Res.* 2009;336(1):79-89.
63. Lindsley A, et al. Identification and characterization of a novel Schwann and outflow tract endocardial cushion lineage-restricted periostin enhancer. *Dev Biol.* 2007;307(2):340-355.
64. Li G, et al. Phosphatidylinositol-3-kinase signaling mediates vascular smooth muscle cell expression of periostin in vivo and in vitro. *Atherosclerosis.* 2006;188(2):292-300.
65. Gelati M, Aplin AC, Fogel E, Smith KD, Nicosia RF. The angiogenic response of the aorta to injury and inflammatory cytokines requires macrophages. *J Immunol.* 2008;181(8):5711-5719.
66. Koh W, Stratman AN, Sacharidou A, Davis GE. In vitro three dimensional collagen matrix models of endothelial lumen formation during vasculogenesis and angiogenesis. *Methods Enzymol.* 2008;443:83-101.

OPEN ACCESS Freely available online PLoS one

Gene Knock-Outs of Inositol 1,4,5-Trisphosphate Receptors Types 1 and 2 Result in Perturbation of Cardiogenesis

Keiko Uchida[1]¶, Megumi Aramaki[1]¶, Maki Nakazawa[1], Chihiro Yamagishi[1], Shinji Makino[2], Keiichi Fukuda[2], Takeshi Nakamura[3]†, Takao Takahashi[1], Katsuhiko Mikoshiba[3,4]*, Hiroyuki Yamagishi[1]*

1 Department of Pediatrics, Keio University School of Medicine, Tokyo, Japan, **2** Department of Regenerative Medicine and Advanced Cardiac Therapeutics, Keio University School of Medicine, Tokyo, Japan, **3** Calcium Oscillation Project, ICORP-SORST, Japan Science and Technology Agency, Saitama, Japan, **4** Laboratory for Developmental Neurobiology, Brain Science Institute (BSI), RIKEN, Saitama, Japan

Abstract

Background: Inositol 1,4,5-trisphosphate receptors (IP_3R1, 2, and 3) are intracellular Ca^{2+} release channels that regulate various vital processes. Although the ryanodine receptor type 2, another type of intracellular Ca^{2+} release channel, has been shown to play a role in embryonic cardiomyocytes, the functions of the IP_3Rs in cardiogenesis remain unclear.

Methodology/Principal Findings: We found that $IP_3R1^{-/-}$-$IP_3R2^{-/-}$ double-mutant mice died *in utero* with developmental defects of the ventricular myocardium and atrioventricular (AV) canal of the heart by embryonic day (E) 11.5, even though no cardiac defect was detectable in $IP_3R1^{-/-}$ or $IP_3R2^{-/-}$ single-mutant mice at this developmental stage. The double-mutant phenotype resembled that of mice deficient for calcineurin/NFATc signaling, and NFATc was inactive in embryonic hearts from the double knockout-mutant mice. The double mutation of *$IP_3R1/R2$* and pharmacologic inhibition of IP_3Rs mimicked the phenotype of the AV valve defect that result from the inhibition of calcineurin, and it could be rescued by constitutively active calcineurin.

Conclusions/Significance: Our results suggest an essential role for IP_3Rs in cardiogenesis in part through the regulation of calcineurin-NFAT signaling.

Citation: Uchida K, Aramaki M, Nakazawa M, Yamagishi C, Makino S, et al. (2010) Gene Knock-Outs of Inositol 1,4,5-Trisphosphate Receptors Types 1 and 2 Result in Perturbation of Cardiogenesis. PLoS ONE 5(9): e12500. doi:10.1371/journal.pone.0012500

Editor: David E. Clapham, Harvard Medical School, United States of America

Received April 23, 2010; **Accepted** July 26, 2010; **Published** September 1, 2010

Funding: This work was supported by a Grant-in-Aid for Scientific Research (H.Y.) and a Grant-in-Aid for Young Scientists (K.U.) from the Ministry of Education, Culture, Sports, Science and Technology, Japan, the Pfizer Fund for Development Research (H.Y.), and a Research Fund from the Japan Automobile Association (H.Y.). The funders had no role in study design, data collection and analysis, decision to publish, or preparation of the manuscript.

Competing Interests: The authors have declared that no competing interests exist.

* E-mail: mikosiba@brain.riken.jp (KM); hyamag@sc.itc.keio.ac.jp (HY)

¶ These authors contributed equally to this work.

† Deceased.

Introduction

Intracellular Ca^{2+} signaling is crucial for cardiac functions [1]. Two types of Ca^{2+} release channels on the sarcoplasmic/endoplasmic reticulum (SR/ER) serve to regulate Ca^{2+} release from intracellular Ca^{2+} stores: the ryanodine receptor (RyR) and inositol 1,4,5-trisphosphate receptor (IP_3R). RyR is mainly required for physiologic excitation–contraction coupling in the heart, whereas IP_3R mediates Ca^{2+} mobilization, in response to IP_3 produced by phospholipase C activation, not only in most non-excitable cells but also in excitable cells including cardiomyocytes [2]. There have been identified three subtype of IP_3Rs (IP_3R1, IP_3R2 and IP_3R3), derived from three distinct genes in mammals [3,4]. We previously generated mice that lacked IP_3R1, IP_3R2 and IP_3R3 by disrupting the corresponding gene within the first exon [5,6], and reported the cerebellar phenotype of $IP_3R1^{-/-}$ mice [5] and the pancreatic phenotype of $IP_3R2^{-/-}$-$IP_3R3^{-/-}$ mice [6], thereby demonstrating the specific and redundant roles of IP_3Rs in organ development and function. Regarding the heart, each *IP_3R1*, *IP_3R2*, and *IP_3R3* single-mutant mouse showed normal cardiogenesis, in contrast to the ryanodine receptor type 2 single-mutant mouse, which showed embryonic lethality owing to dysfunction of the SR in the embryonic cardiomyocyte [7].

Extracellular ligands binding to many receptors, including G-protein coupled receptors and tyrosine-kinase coupled receptors, lead to a transient release of Ca^{2+} from ER/SR, through IP_3Rs. IP_3-induced Ca^{2+} release concurrently results in depletion of intracellular Ca^{2+} store, which triggers Ca^{2+} release activated Ca^{2+} (CRAC) channels [8]. Subsequent increase of cytosolic $[Ca^{2+}]$ through CRAC channels activates several Ca^{2+}- binding proteins, including calcineurin, which in turn dephosphorylates and induces the nuclear localization of the nuclear factor of activated T cells (NFAT) transcription complexes [9]. During heart development, NFATc1 is expressed in the endocardium of the AV canal that will make up the endocardial cushion [10]. NFATc1 knockout embryos show abnormal valvulogenesis [11,12], while NFATc2/

3/4 triple knockout embryos and calcineurin-deficient embryos demonstrate impaired endocardial cushion formation, thinning of ventricular myocardium and dysregulation of vascular development [10,13,14]. To determine the function of the intracellular Ca^{2+} signaling cascade via IP_3Rs in the embryonic hearts, here we generated and analyzed IP_3R1 and IP_3R2-deficient mice. Our findings support an essential redundant role of IP_3R1 and IP_3R2 during cardiogenesis, possibly implicating the calcineurin/NFAT signaling pathway.

Results

Overlapping Expression Patterns of IP_3R1 and IP_3R2 in Embryonic Hearts

Firstly, we examined the normal pattern of expression of the IP_3Rs by RNA *in situ* hybridization. Consistent with a previous report [15], expression of IP_3R1 mRNA was detected at embryonic day (E)8.5 in the heart, where it was enhanced in the posterior part of the primitive heart, including the atrium (Fig. 1*A*). IP_3R1 mRNA expression extended to the ventricles through the AV canal at E9.5–10.5 (Fig. 1*A*). In contrast, IP_3R2 mRNA expression was not detected at E8.5 but was detected at E9.5 throughout the heart, including the atrium, AV canal, and ventricles (Fig. 1*B*). These expression signals were not detected by sense riboprobes as a control (data not shown). Quantitative RT-PCR using total RNA extracted from hearts at E8.5 to E16.0 and western blot analysis of proteins at E9.5 and E12.5 indicated that the IP_3R1 and IP_3R2 transcripts and proteins were expressed at significant levels in the developing hearts (Fig. 1*C* and *D*), consistent with the results of the RNA *in situ* hybridization experiments. We performed an immunohistochemical analysis on sections of the heart at E9.25, E9.75 and E10.5 to determine the cell types in the embryonic heart that express the IP_3R proteins. At E9.25, IP_3R1 was expressed in both endocardial cells and myocardial cells, whereas IP_3R2 was expressed dominantly in endocardial cells (Fig. 1*E*). Co-expression of IP_3R1 and IP_3R2 was observed in the endocardial cells of the AV canal (Fig. 1*E*). At E9.75 to E10.5, the expression of IP_3R2 expanded to the myocardium and IP_3R1 and IP_3R2 were co-expressed not only in the endocardial cells but also in the myocardial cells (Fig. 1*E*). These expression signals with anti- IP_3R1 and anti- IP_3R2 antibodies were not detected in the sections of the $IP_3R1^{-/-}$-$IP_3R2^{-/-}$ double-mutant embryos as a control (data not shown).

Cardiac Defects in $IP_3R1^{-/-}$-$IP_3R2^{-/-}$ Double-Mutant Mice

To explore further the roles of the IP_3Rs in cardiac development, we delineated the cardiac phenotype of the IP_3R mutant mouse. $IP_3R1^{-/-}$-$IP_3R2^{-/-}$ double-mutant mice showed embryonic lethality by E11.5 (see supporting information (SI) Table S1) with heart defects, while either $IP_3R1^{+/-}$-$IP_3R2^{-/-}$ or $IP_3R1^{-/-}$-$IP_3R2^{+/+}$ mouse developed normally through E11.5. The $IP_3R1^{-/-}$-$IP_3R2^{-/-}$ double-mutant mice began to show growth retardation at E9.5, although they appeared normal by E9.25 and had regular cardiac contractions comparable to those of wild-type. Detailed analysis of mouse hearts at E9.75 showed that the ventricles of $IP_3R1^{-/-}$-$IP_3R2^{-/-}$ mice were more transparent than those of $IP_3R1^{+/-}$-$IP_3R2^{-/-}$ mice, even though comparable 29 pairs of somites were developed, cardiac looping occurred normally, and morphologic atria and ventricles were apparent in both $IP_3R1^{-/-}$-$IP_3R2^{-/-}$ mice and $IP_3R1^{+/-}$-$IP_3R2^{-/-}$ mice (Fig. 2*A*). Histological analysis revealed thin myocardial walls and poor trabeculation in the ventricles of $IP_3R1^{-/-}$-$IP_3R2^{-/-}$ mice at E9.75 (Fig. 2*B*). Together with the ventricular abnormalities, hypocellularity in the cushion of AV canal was documented in the $IP_3R1^{-/-}$-$IP_3R2^{-/-}$ hearts (Fig. 2*B*). Taken together with the evidence of overlapping expression of IP_3R1 and IP_3R2 in the developing ventricles and AV canal at E9.5 or later, these results suggest that these two genes play redundant roles in cardiogenesis. Although histologic abnormalities were noted, analysis using electron microscopy found no structural defects in the subcellular organelles, in the $IP_3R1^{-/-}$-$IP_3R2^{-/-}$ hearts at E9.5 (Fig. S1).

We performed a molecular analysis to investigate the association between the $IP_3R1^{-/-}$-$IP_3R2^{-/-}$ double-mutant phenotype and the differentiation of atrial and ventricular cardiomyocytes. Nkx2.5, Mlc2a, and Mlc2v are the earliest markers of cardiomyocyte differentiation in the atrium and ventricle during cardiogenesis [16,17,18]. These markers were expressed at normal levels in $IP_3R1^{-/-}$-$IP_3R2^{-/-}$ hearts at E9.5 (Fig. S2). Markers for the right ventricle (Hand2 [19]), left ventricle (Hand1 [19]) and both ventricles (Hrt2 [20]) were also expressed normally in $IP_3R1^{-/-}$-$IP_3R2^{-/-}$ hearts at E9.5 (Fig. S2). These results suggest that cardiomyocyte differentiation and the specification of both ventricles occur normally in $IP_3R1^{-/-}$-$IP_3R2^{-/-}$ hearts despite poor formation of the ventricles.

In spite of the well-developed organs other than hearts in $IP_3R1^{-/-}$-$IP_3R2^{-/-}$ embryos the early embryonic lethality of $IP_3R1^{-/-}$-$IP_3R2^{-/-}$ mice and a previous report on the requirement for certain isotypes of phospholipase C_δ that produce IP_3 for placentation [21,22] led us to investigate the possibility of placental defects in $IP_3R1^{-/-}$-$IP_3R2^{-/-}$ mice. Histologic analysis revealed that the embryonic vessels elongated and contact with the maternal blood vessels in the $IP_3R1^{-/-}$-$IP_3R2^{+/-}$ or $IP_3R1^{+/-}$-$IP_3R2^{-/-}$ placentas at E9.5. The area of the labyrinth layer, which comprises a network of embryonic and maternal blood vessels, was significantly smaller in the $IP_3R1^{-/-}$-$IP_3R2^{-/-}$ placenta than that in the $IP_3R1^{+/-}$-$IP_3R2^{-/-}$ placenta at E9.5 (Fig. S3).

Downregulated Cell Proliferation Activity in $IP_3R1^{-/-}$-$IP_3R2^{-/-}$ Double-Mutant Ventricles

Next, we looked in the ventricles of $IP_3R1^{-/-}$-$IP_3R2^{-/-}$ mice at E9.5 for cell proliferation markers using the anti-phospho-histone H3 (PH3) antibody and 5-bromo-2′-deoxy-uridine (BrdU), and performed the TUNEL assay for apoptosis (Fig. 3 *A* and *B*). The numbers of PH3-positive cells and BrdU-incorporated cells were lower in the $IP_3R1^{-/-}$-$IP_3R2^{-/-}$ ventricular endocardium and myocardium than in those of $IP_3R1^{+/-}$-$IP_3R2^{-/-}$ hearts, whereas the numbers of proliferating cells in the pharyngeal arch and the numbers of apoptotic signals detected by the TUNEL assay were similar between $IP_3R1^{-/-}$-$IP_3R2^{-/-}$ and $IP_3R1^{+/-}$-$IP_3R2^{-/-}$ embryos (Fig. 3*A* and *B*). These results indicate that the redundant functions of IP_3R1 and IP_3R2 are essential for ventricular cell proliferation. The $IP_3R1^{-/-}$-$IP_3R2^{-/-}$ mouse phenotype is similar to that of mice lacking both Ca^{2+}-sensitive transcription factors, NFATc3 and NFATc4, where the proliferation of the ventricular cells is considerably reduced [14].

IP_3R1 and IP_3R2 Redundantly Control Endocardial Cushion Development through Calcineurin/NFATc Signaling

Histological analyses of the developing hearts were performed using alcian blue staining, which detects acidic mucosubstances, as well as staining with biotinylated hyaluronan binding protein for visualizing hyaluronan production (Fig. 4*A*). These analyses revealed the absence of mesenchymal cells in the cushion of the AV canal of $IP_3R1^{-/-}$-$IP_3R2^{-/-}$ mice at E9.5, whereas the

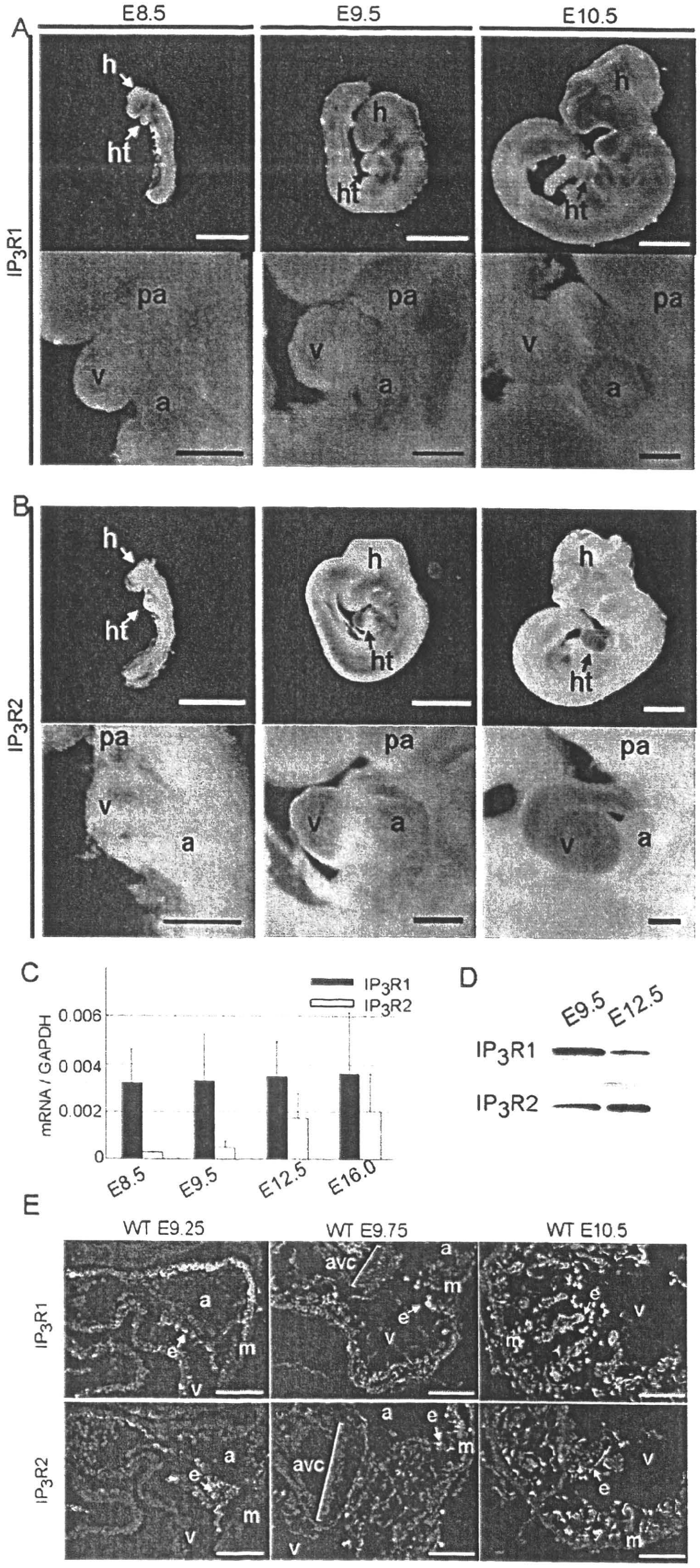
A
E8.5
E9.5
E10.5
IP$_3$R1
h
ht
pa
v
a
B
IP$_3$R2
C
mRNA / GAPDH
0.006
0.004
0.002
0
E8.5
E9.5
E12.5
E16.0
IP$_3$R1
IP$_3$R2
D
E9.5
E12.5
IP$_3$R1
IP$_3$R2
E
WT E9.25
WT E9.75
WT E10.5
IP$_3$R1
IP$_3$R2
avc
a
m
e
v

Figure 1. Both IP_3R1 and IP_3R2 are expressed in the embryonic heart. (*A, B*) Whole-mount *in situ* hybridization using IP_3R1 (*A*) and IP_3R2 (*B*) antisense riboprobes at E8.5, E9.5, and E10.5. Whole-mount views (upper panels) and close-up views of the hearts (lower panels) are shown. Scale bars: 1 mm (whole-mount views) and 0.2 mm (heart close-up views). (*C*) Quantitative RT-PCR of IP_3R1 (black bars) and IP_3R2 (gray bars) using total RNA samples extracted from embryonic hearts at E8.5 to E16.0. Error bars indicate standard deviations. (*D*) Western blot of embryonic hearts with anti-IP_3R1 (18A10) and anti-IP_3R2 (KM1083) antibodies. Lysates (10 µg) of hearts at E9.5 and E12.5 were analyzed. The protein contents of the heart extracts were determined by the Bradford method. (*E*) The transverse sections of the wildtype embryos at E9.25, E9.75 and E10.5 were immunostained with the anti-IP_3R1 (upper panels) and anti-IP_3R2 (lower panels) antibodies. Scale bars: 0.1 mm. a, atrium; avc, atrioventricular canal; e, endocardium; h, head; ht, heart; m, myocardium; pa, pharyngeal arch; v, ventricle.
doi:10.1371/journal.pone.0012500.g001

volume and content of the cardiac jelly in the $IP_3R1^{-/-}$-$IP_3R2^{-/-}$ hearts were comparable with those in the $IP_3R1^{+/-}$-$IP_3R2^{-/-}$ hearts. Expression of the transcription factor Tbx2 was also normal in the AV canals of $IP_3R1^{-/-}$-$IP_3R2^{-/-}$ mice, which suggests that specification and differentiation of the AV canal is unaffected in the mutant mice (Fig. 4*A*). These findings led us to hypothesize that IP_3R1 and IP_3R2 were required for the epithelial-mesenchymal transformation (EMT) in the developing AV cushion. To determine whether IP_3R-mediated Ca^{2+} signaling could affect the process of EMT in the AV cushion, we performed an *in vitro* EMT assay [23]. The E9.5 wild-type AV canal tissues were explanted and treated with 2-aminoethoxydiphenyl borate (2APB) onto a collagen gel, which is a non-selective membrane-permeable inhibitor of IP_3Rs and CRAC channels [24]. After 24 h

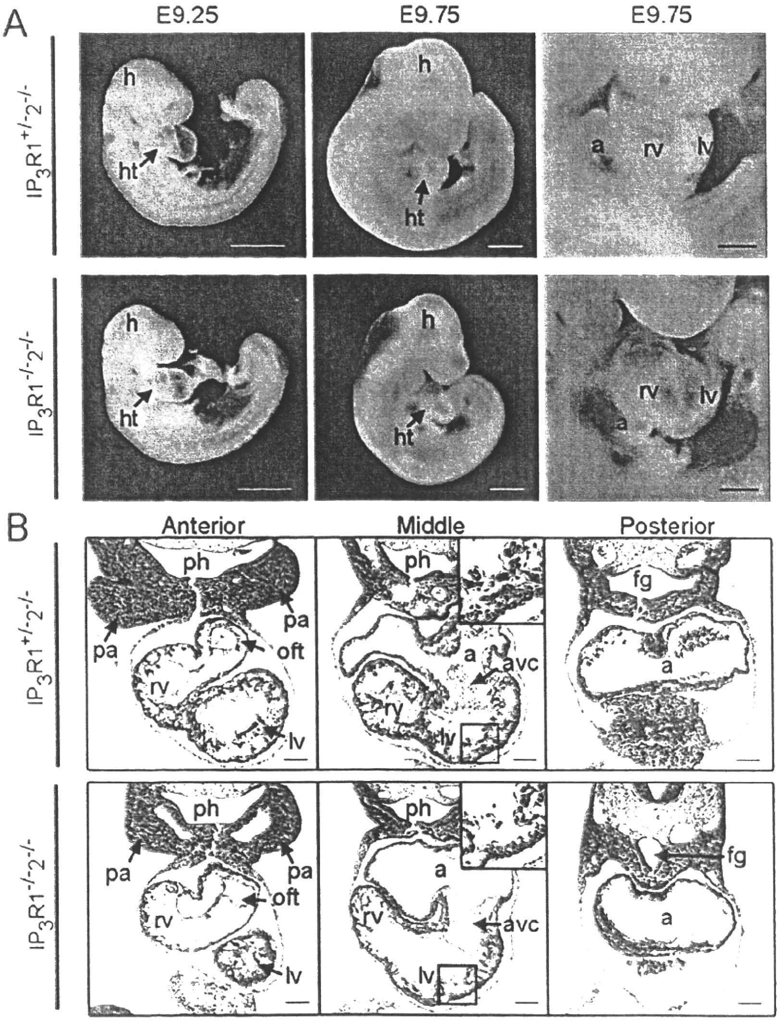

Figure 2. Cardiac defects in $IP_3R1^{-/-}$-$IP_3R2^{-/-}$ mice. (*A*) The morphologies of the embryos and developing hearts of $IP_3R1^{+/-}$-$IP_3R2^{-/-}$ (upper panels) and $IP_3R1^{-/-}$-$IP_3R2^{-/-}$ (lower panels) mice at E9.25 and at E9.75. Scale bars, 0.5 mm (whole-mount views) and 0.2 mm (heart close-up views). (*B*) Hematoxylin and eosin-stained transverse sections of the anterior, middle and posterior segments of the hearts of $IP_3R1^{+/-}$-$IP_3R2^{-/-}$ (upper panels) and $IP_3R1^{-/-}$-$IP_3R2^{-/-}$ (lower panels) mice at E9.75. The insets in the middle panels are higher-magnification images of the boxed areas. Scale bars, 0.2 mm. a, atrium; avc, atrioventricular canal; fg, foregut; h, head; ht, heart; lv, left ventricle; oft, outflow tract; pa, pharyngeal arch; ph, pharynx; rv, right ventricle.
doi:10.1371/journal.pone.0012500.g002

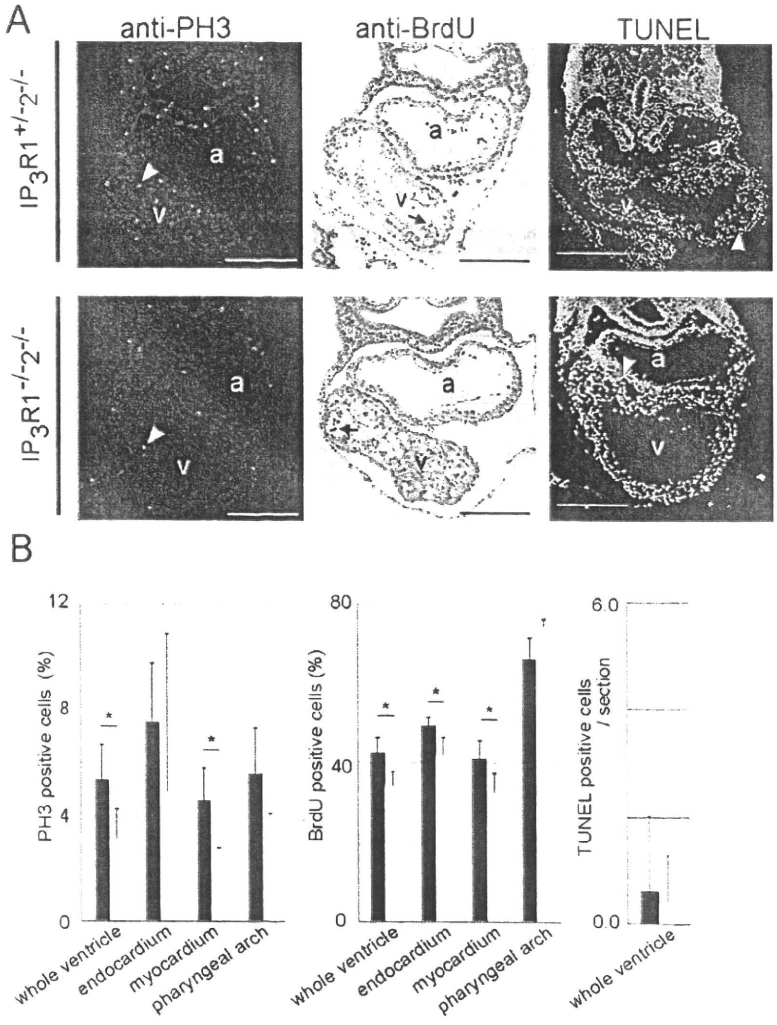

Figure 3. IP_3R1 and IP_3R2 redundantly regulate cardiomyocyte proliferation in the developing ventricles. (*A*) Transverse sections of E9.5 $IP_3R1^{+/-}$-$IP_3R2^{-/-}$ (upper panels) and $IP_3R1^{-/-}$-$IP_3R2^{-/-}$ (lower panels) embryos that were immunostained with the anti-phospho-histone H3 (PH3) antibody, immunostained with the anti-BrdU antibody after injection of BrdU, and subjected to the TUNEL assay. The green signals (white arrowheads) in the left panels, brown signals in the middle panels (arrows) and yellow signals (white arrowheads) in the right panels indicate the nuclei of the PH3-, BrdU-, and TUNEL-positive cells, respectively. Scale bars, 0.2 mm. a, atrium; v, ventricle. (*B*) The left and middle graphs show the percentages of proliferating cells in the whole ventricles, the endocardium and myocardium of the ventricles, and the pharyngeal arches of $IP_3R1^{-/-}$-$IP_3R2^{-/-}$ mutants (gray bars), compared with those of $IP_3R1^{+/-}$-$IP_3R2^{-/-}$ controls (black bars) ($*P<0.05$, n = 3). The right graph shows the number of apoptotic cells ($P = 0.45$, n = 7). Error bars indicate standard deviations.
doi:10.1371/journal.pone.0012500.g003

of treatment with 2APB, EMT was inhibited, resulting in a significant decrease in the number of cells that transformed and migrated into the collagen gel compared with control explants treated with DMSO (Fig. 4*B*). Similarly, EMT was significantly inhibited in the AV canal explants from $IP_3R1^{-/-}$-$IP_3R2^{-/-}$ embryo at E9.5 (Fig. 4*B*).

Of the several signaling pathways implicated in AV cushion and myocardial development, we focused on calcineurin/NFAT signaling because of the similarities noted between the phenotypes of the $IP_3R1^{-/-}$-$IP_3R2^{-/-}$ mice and calcineurin- or *NFATc*-deficient mice [10,13,14]. To determine whether IP_3R1 and IP_3R2 regulate intracellular Ca^{2+} signaling upstream of calcineurin/NFATc, we examined the cellular localization of NFATc1 in the AV canals of $IP_3R1^{-/-}$-$IP_3R2^{-/-}$ mice. Immunohistochemical analysis revealed that NFATc1 failed to translocate into the nuclei of the endocardial cells in the AV canals of $IP_3R1^{-/-}$-$IP_3R2^{-/-}$ mice at E9.5, and that the expression of NFATc1 was downregulated by E10.5 (Fig. 4*C*). Nuclear translocation of NFATc1 appeared normal at E9.25 but was inhibited from E9.5 (Fig. S4). Next, we examined the activation of NFATc4 by western blot analysis using the lysates from $IP_3R1^{-/-}$-$IP_3R2^{-/-}$ hearts at 9.75. The quantity of the dephosphorylated form of NFATc4 was decreased in the $IP_3R1^{-/-}$-$IP_3R2^{-/-}$ heart compared to the $IP_3R1^{+/-}$-$IP_3R2^{-/-}$ heart (Fig. 4*D*). These observations are reminiscent of those made for calcineurin B*/* mice, in which the activation of calcineurin B is disrupted [13]. To provide further evidence for the possible interaction between IP_3Rs and calcineurin/NFATc signaling, we tested whether constitutively

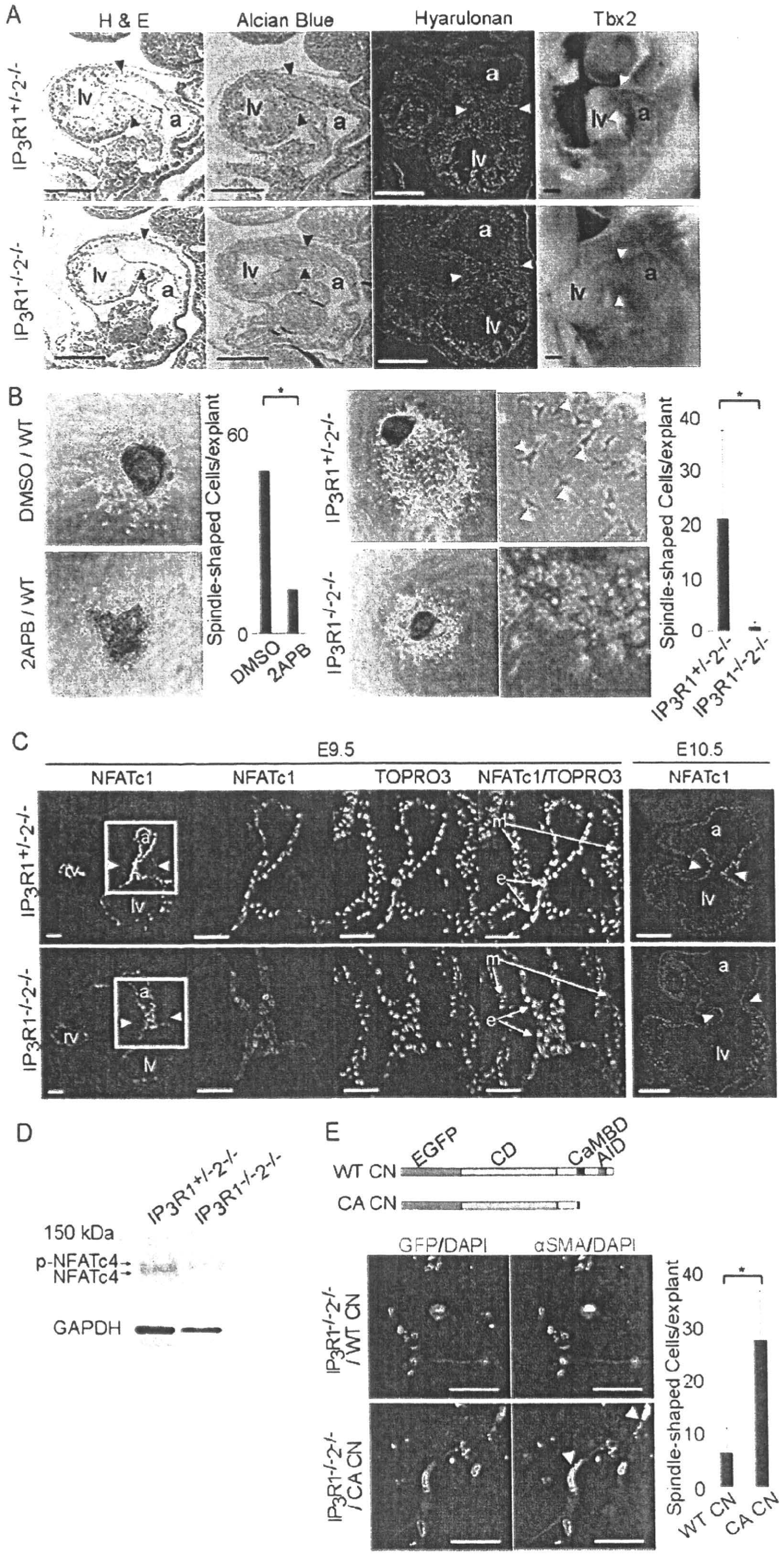
A
H & E
Alcian Blue
Hyarulonan
Tbx2
IP3R1+/-2-/-
IP3R1-/-2-/-
lv
a
B
DMSO / WT
2APB / WT
Spindle-shaped Cells/explant
60
0
DMSO
2APB
*
IP3R1+/-2-/-
IP3R1-/-2-/-
40
30
20
10
0
C
E9.5
E10.5
NFATc1
NFATc1
TOPRO3
NFATc1/TOPRO3
NFATc1
rv
m
e
D
IP3R1+/-2-/-
IP3R1-/-2-/-
150 kDa
p-NFATc4
NFATc4
GAPDH
E
WT CN
CA CN
EGFP
CD
CaMBD
AID
GFP/DAPI
αSMA/DAPI
IP3R1-/-2-/- /WT CN
IP3R1-/-2-/- /CA CN
WT CN
CA CN

Figure 4. IP_3Rs are essential for EMT through calcineurin activity during endocardial cushion development in mice. (*A*) Hematoxylin and eosin staining, alcian blue staining, staining with biotinylated hyaluronan binding protein and whole-mount *in situ* hybridization for a marker of the atrioventricular (AV) myocardium (Tbx2) of $IP_3R1^{+/-}$-$IP_3R2^{-/-}$ (upper panels) and $IP_3R1^{-/-}$-$IP_3R2^{-/-}$ (lower panels) embryos at E9.5. Mesenchymal cells are absent from the $IP_3R1^{-/-}$-$IP_3R2^{-/-}$ AV cushion (arrowheads), whereas the staining levels for alcian blue (blue signals), hyaluronan (green signals) and Tbx2 (purple signals) are not altered. Scale bars, 0.1 mm. (*B*) *In vitro* EMT assay using the endocardial cushion from the AV canal. The left panels show that treatment of wild-type (WT) cushion explants with the IP_3R inhibitor 2APB inhibits the outgrowth of spindle-shaped cells as compared with the control treatment (DMSO). The right panels show the $IP_3R1^{+/-}$-$IP_3R2^{-/-}$ and the $IP_3R1^{-/-}$-$IP_3R2^{-/-}$ AV cushion explants. The higher magnification views of the explants are shown besides. The spindle-shaped cells migrating into collagen gel are indicated with yellow arrowheads. The number of the spindle-shaped migrating cells is significantly lower in the culture that contains 2APB (left graph) and in the culture from the $IP_3R1^{-/-}$-$IP_3R2^{-/-}$ AV cushion (right graph) (*$P<0.05$, n = 3). Error bars indicate standard deviations. (*C*) Transverse sections at the level of the AV canal stained with the anti-NFATc1 antibody and TOPRO3 show impairment of translocation of NFATc1 into nuclei at E9.5. The expression level of NFATc1 is decreased at E10.5 in $IP_3R1^{-/-}$-$IP_3R2^{-/-}$ hearts. Scale bars, 0.05 mm. Arrowheads indicate the AV canal and higher-magnification images of the boxed area. (*D*) Western blot analysis with anti-NFATc4 antibody using heart lysates of the wildtype and the $IP_3R1^{-/-}$-$IP_3R2^{-/-}$ embryos at E9.75. Blotting with anti-GAPDH antibody on each lane was used as a loading control. The inactive form of NFATc4 (p-NFATc4) remained and active form (NFATc4) was reduced in $IP_3R1^{-/-}$-$IP_3R2^{-/-}$ hearts compared to $IP_3R1^{+/-}$-$IP_3R2^{-/-}$ hearts. (*E*) The structures of the wildtype calcineurin (WT CN) and the constitutively active form of calcineurin (CA CN) cDNA are shown. Infection with CA CN cDNA resulted in significant increase in the number of the spindle-shaped and α smooth muscle actin (αSMA)-positive cells (yellow arrowheads) in the culture of $IP_3R1^{-/-}$-$IP_3R2^{-/-}$ AV cushion explants (*$P<0.05$, n = 4). a, atrium; e, endocardium; lv, left ventricle; m, myocardium, rv, right ventricle; v, ventricle.

doi:10.1371/journal.pone.0012500.g004

active calcineurin could rescue the phenotype of $IP_3R1^{-/-}$-$IP_3R2^{-/-}$. Infection of cytomegalovirus-associated constitutively active calcineurin, which can be activated independently of Ca^{2+} increase by deletion of its calmodulin binding domain and autoinhibitory domain [25], significantly restored the EMT activity in $IP_3R1^{-/-}$-$IP_3R2^{-/-}$ AV explants (Fig. 4*E*). Taken together, our results indicate that IP_3R1 and IP_3R2, at least in part, redundantly activate and maintain calcineurin/NFATc signaling.

To investigate further whether IP_3R-mediated Ca^{2+} signaling is required for AV cushion development, we utilized a relatively simple model of heart development in zebrafish treated with an inhibitor of IP_3R (Fig. 5*A*). As described previously [10], treatment with the calcineurin inhibitors cyclosporine A (CsA) or FK506 between 24 h and 33 h postfertilization (hpf) affects AV cushion development and heart valve formation in zebrafish. Intriguingly, treatment with 2APB between 24 hpf and 33 hpf disrupted AV cushion development in zebrafish (Fig. 5*A*) in a dose-dependent fashion (Fig. 5*B*). This results in a massive regurgitation of the AV valve and heart failure with pericardial effusion reminiscent of treatment with CsA (Fig. 5*A* and Video S1). Although myocardial development appeared normal by staining of the sarcomeric protein MF20, disruption of AV canal cushion development, and possibly decreased myocardial function, was common in CsA-treated and 2APB-treated zebrafish (Fig. 5*A* and *B*). These data further support that IP_3R-mediated signaling is essential for AV cushion development, possibly implicating the calcineurin/NFAT signaling across species.

Discussion

In the present study, we used a series of molecular, pharmacologic and genetic manipulations in mice and zebrafish to demonstrate that IP_3Rs are involved in the local control of Ca^{2+} that is necessary to activate the calcineurin-NFATc signaling pathway required for cardiogenesis. To date, it has been shown that calcineurin/NFATc signaling has an important role for AV cushion formation, valvulogenesis, and cardiomyocyte development [10,11,12,14], however, the process by which this signaling is activated by Ca^{2+} has not been elucidated. In *Xenopus* embryos, NFAT is a downstream effecter of the IP_3-Ca^{2+} signal during dorsoventral axis formation [26]. In mammals, IP_3Rs act upstream of calcineurin/NFAT signaling in T lymphocytes *in vitro* [27]. In this study, we have indentified that IP_3R1 and IP_3R2 may exist, at least in part, upstream of calcineurin/NFATc signaling during heart development. Our data provide new insights into the way how Ca^{2+} signals regulate Ca^{2+}-binding molecules essential for cardiogenesis, such as the Ca^{2+} dependent phosphatase, calcineurin.

Here, we have shown several lines of findings that support that the IP_3R-mediated Ca^{2+} signaling may be implicated in the calcineurin/NFATc signaling pathway although it is difficult to clarify whether IP_3Rs may directly activate calcineurin during cardiogenesis. We showed that NFATc1 and NFATc4 were not activated in $IP_3R1^{-/-}$-$IP_3R2^{-/-}$ mice at E9.5 (Fig. 4*C* and *D*), and that the expression of NFATc1 was downregulated by E10.5 (Fig. 4*C*), using immunohistological and biochemical experiments. Moreover, we showed that the disturbance of endocardial cushion development in $IP_3R1^{-/-}$-$IP_3R2^{-/-}$ embryos could be rescued by addition of constitutively active calcineurin (Fig. 4*E*). These data indicate that IP_3R1 and IP_3R2 may, directly or indirectly, function redundantly in the activation of calcineurin/NFAT signaling. Vascular endothelial growth factor (VEGF), inducing NFATc1 nuclear translocation, markedly increases the proliferation of valve endothelial cells *in vitro* [28]. The VEGF receptor tyrosine kinase activating phospholipase Cγ- IP_3 signal triggers intracellular Ca^{2+} increase [29], suggesting that VEGF might be a candidate of extracellular signals upstream of IP_3Rs-NFATc1 activation in the endocardium. Failure of nuclear translocation and downregulation of NFATc1 is probably due to disruption of some of the following positive feedback mechanisms: 1) NFATc1-binding to the promoter/enhancer of the *NFATc* gene [30]; 2) activation of calcineurin transcription by NFATc [31]; and 3) induction of the IP_3R1 gene as previously documented in neurons [32].

We also showed that the phenotype of $IP_3R1^{-/-}$-$IP_3R2^{-/-}$ embryos involved that of the *NFATc2/3/4* knockout mice [10,13,14] and was much more severe than that of the *NFATc1* null mice [11,12]. Therefore, it is likely that IP_3R-mediated Ca^{2+} signaling during cardiogenesis regulates NFATc family members in addition to NFATc1 as well as unknown downstream targets other than the calcineurin/NFATc signaling pathway. It is also unclear whether endocardial or myocardial cells are primarily affected in the $IP_3R1^{-/-}$-$IP_3R2^{-/-}$ embryos. In characterizing the role of this pathway in heart development, our study revealed the co-expression and involvement of IP_3R1 and IP_3R2 in the development of both endocardial and myocardial cells. Unequivocal answer about the functions of IP_3R1 and IP_3R2 for cardiac development awaits further study of cell-specific conditional knockout mice.

Although our experiments in AV explants and in zebrafish using 2APB support our hypothesis led by our experiments using $IP_3R1^{-/-}$-$IP_3R2^{-/-}$ mice, there is a limitation for using 2APB.

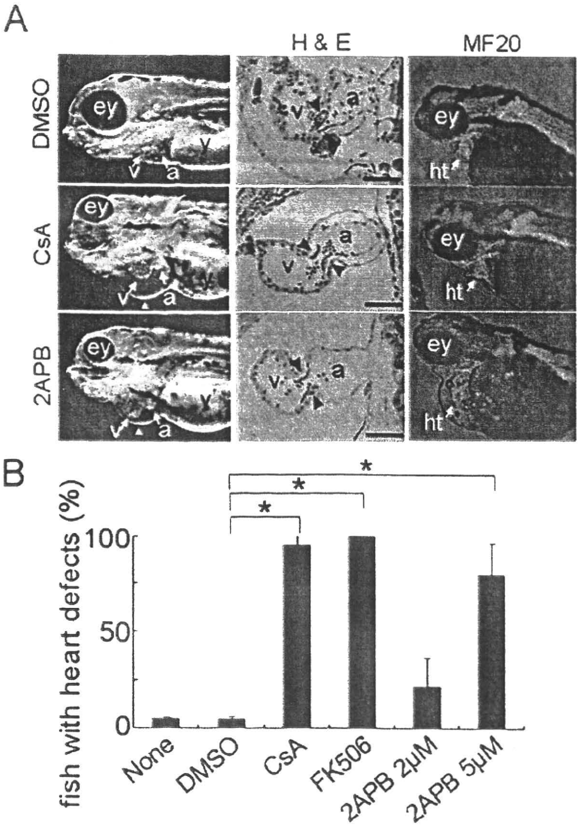

Figure 5. Inhibition of IP_3Rs and calcineurin results in a common developmental defect in zebrafish hearts. (*A*) The left panels show the gross abnormalities in the hearts of zebrafish treated with DMSO, CsA (calcineurin inhibitor), and 2APB (IP_3R inhibitor). Atrioventricular regurgitation is induced by the addition of CsA and 2APB, resulting in heart failure with pericardial swelling (yellow arrowheads). The middle panels show the histologic abnormalities including a decrease in the number of cushion cells in the atrioventricular valves (arrowheads). The right panels show the expression of sarcomeric protein MF20 in zebrafish hearts that did not alter with CsA- or 2APB-treatment. (*B*) The significant increase in the number of zebrafish with pericardial swelling following the addition of CsA, FK506, or 2APB, is indicated in the graph ($^*P<0.05$, n = 3). Error bars indicate standard deviations. a, atrium; ey, eye; ht, heart; v, ventricle; y, yolk.
doi:10.1371/journal.pone.0012500.g005

Because 2APB is non-selective inhibitor, it is a potent CRAC channel inhibitor in addition to having an inhibitory effects on not only IP_3R1 and IP_3R2, but also other subtype of IP_3R [33]. Unfortunately, there is no selective IP_3R inhibitor presently available. The observed defect in AV explants and in zebrafish with 2APB should include the possible effects of 2APB on CRAC channel activity, although AV explants from $IP_3R1^{-/-}$-$IP_3R2^{-/-}$ mice showed similar defect. There also is a limitation to determine the cause of death in the $IP_3R1^{-/-}$-$IP_3R2^{-/-}$ mice in this study. The placental defect, in conjunction with the cardiac defect, are likely to account for embryonic lethality in these mice, however, we could neither correctly estimate impact of each defect nor rule out defects of other organs. Further strategy for inactivation of the specific IP_3R in specific tissues and organs would be required to overcome these limitations appeared in this study.

The DSCR1/MCIP1 gene encoding a calcineurin inhibitor is located on human chromosome 21 and a reduction of NFATc activity is associated with a 1.5-fold increase in gene dosage of DSCR1 and many of the features of Down (Trisomy 21) syndrome, including AV canal defects [34]. The balance between Ca^{2+}-sensitive positive (e.g., IP_3Rs) and negative (e.g., DSCR1) regulation of NFATc may be crucial for organogenesis. Understanding the novel roles of IP_3R-mediated Ca^{2+} signaling opens new avenues of research regarding the molecular embryology of the heart, which may lead to regenerative interventions for patients with congenital heart defects.

Materials and Methods

Animals

$IP_3R1/2$ double-knockout mice were generated by intercrossing $IP_3R1^{+/-}$-$IP_3R\ 2^{-/-}$ paired mice [5,6]. Genomic DNA samples prepared from tail biopsies or yolk sacs were subjected to PCR for genotyping, as described previously [5,6]. Zebrafish (*Danio rerio*) embryos were obtained from the natural spawning of a wild-type ABK line. CsA (50 μg/mL) or 2APB (5 μM) was added between 24 hpf and 33 hpf, and the zebrafish were harvested at 72 hpf for analysis [10]. All experimental procedures and protocols were approved by the animal care and use committees of Keio University (the approval number 09122-(3)) and conformed to the National Institutes of Health *Guidelines for the Care and Use of Laboratory Animals*.

Western Blotting, Quantitative RT-PCR, Whole-Mount *in situ* Hybridization, and Immunohistochemistry

Total heart extracts (10 μg) from E9.5 and E12.5 mice were subjected to 5% SDS-PAGE and analyzed by western blotting with anti-IP_3R1 (18A10) [35] and anti-IP_3R2 (KM1083) antibodies [36]. For quantitative RT-PCR analysis of IP_3R1 and IP_3R2 expression, cDNAs were synthesized using the High Capacity cDNA Archive kit (Applied Biosystems) from total RNA samples extracted from embryonic hearts or placentas using the RNeasy kit (Qiagen). These cDNAs were used as templates in a TaqMan Real-Time PCR with the ABI 7500 Real-Time PCR system (Applied Biosystems). The data are normalized to the levels obtained for *GAPDH*. The TaqMan probes used for *IP_3R1* and *IP_3R2* were Mm00439917_m1 and Mm00444937_m1 (Applied Biosystems), respectively. The whole-mount RNA *in situ* hybridization and immunohistochemistry were performed as previously described [13,37]. The antibodies used for immunohistochemistry on the sections were: mouse anti-NFATc1 (7A6) monoclonal antibody (1:100; Santa Cruz Biotechnology), anti-phospho-histone H3 (Ser10) antibody (1:100; Upstate), anti-BrdU antibody (1:75; Becton Dickinson), anti-NFATc4 (H-74) antibody (1:250; Santa Cruz Biotechnology) and anti-α smooth muscle actin (1A4) antibody (1:400; Sigma).

EMT Assay

The EMT assay was performed as reported previously [23]. Endocardial cushions from the atrioventricular canal were explanted onto rat-tail collagen gel (BD Biosciences). After 24 h of incubation with 2APB, which is a non-selective inhibitor of IP_3Rs [24], or with DMSO as a control, the total number of mesenchymal cells in each dish was counted. AV canal explants were infected using inactivated adenovirus harboring the gene encoding cytomegalovirus-driven constitutively active calcineurin [25] (Adeno-X ViraTrak Expression System 2, Clontech). After overnight incubation to allow attachment, each explant was incubated with 6.4×10^4 viral particles in culture medium.

Whereupon, the AV explants were cultured for an additional 5 days and then assessed as indicated.

Statistical Analysis

All data are expressed as mean ± s.d. ($n \geq 3$). Statistical analysis was performed using the Student's *t*-test. The results shown are representative of more than three independent experiments.

Supporting Information

Materials and Methods S1

Found at: doi:10.1371/journal.pone.0012500.s001 (0.03 MB DOC)

Table S1 Genotype Distributions of Embryos from $IP_3R1^{+/-}$-$IP_3R2^{-/-}$ Intercrosses.

Found at: doi:10.1371/journal.pone.0012500.s002 (0.03 MB DOC)

Figure S1 The ultrastructures of the subcellular organelles of the $IP_3R1^{-/-}$-$IP_3R2^{-/-}$ mice are comparable with those of the $IP_3R1^{+/-}$-$IP_3R2^{-/-}$ mice. Scale bars, 1 µm. g, golgi; m, mitochondrion; mf, myofilament; n, nucleus; rer, rough endoplasmic reticulum; sr, sarcoplasmic reticulum.

Found at: doi:10.1371/journal.pone.0012500.s003 (1.74 MB TIF)

Figure S2 Expression of site-specific markers in embryonic hearts. Whole-mount *in situ* hybridization images of the left- or right-side of the hearts of E9.5 $IP_3R1^{+/-}$-$IP_3R2^{-/-}$ (upper panels) and $IP_3R1^{-/-}$-$IP_3R2^{-/-}$ (lower panels) embryos. The expression patterns of Nkx2.5, MLC2a, and MLC2v (earliest markers of the embryonic heart), and of Hand2, Hand1 and Hrt2 (markers of the right, left, and both ventricles, respectively) are shown. Scale bars, 0.2 mm. a, atrium; lv, left ventricle; oft, outflow tract; pa, pharyngeal arch; rv, right ventricle.

Found at: doi:10.1371/journal.pone.0012500.s004 (5.26 MB TIF)

Figure S3 Cross-sections of E9.5 placentas from $IP_3R1^{-/-}$-$IP_3R2^{+/-}$ (upper panels), $IP_3R1^{+/-}$-$IP_3R2^{-/-}$ (middle panels) and $IP_3R1^{-/-}$-$IP_3R2^{-/-}$ (lower panels) mutant mice. The widths of the labyrinth area indicated in parentheses. Higher-magnification images of the boxed areas are shown in the right panels. Scale bars, 0.5 mm. The graph shows quantification of the labyrinth areas of the $IP_3R1^{+/-}$-$IP_3R2^{-/-}$ and $IP_3R1^{-/-}$-$IP_3R2^{-/-}$ placentas at E9.5. The area of the $IP_3R1^{-/-}$-$IP_3R2^{-/-}$ labyrinth is significantly lower (*$P<0.05$, n = 3). Error bars indicate standard deviations. ev, embryonic vessel; mv, maternal vessel.

Found at: doi:10.1371/journal.pone.0012500.s005 (5.68 MB TIF)

Figure S4 The percentages of cells with nuclear translocation of NFATc1 in the $IP_3R1^{-/-}$-$IP_3R2^{-/-}$ hearts (white bars) are significantly lower than those in the $IP_3R1^{+/-}$-$IP_3R2^{-/-}$ hearts (black bars) at E9.5 to E10.0 (*$P<0.01$, n = 3). Error bars indicate standard deviations.

Found at: doi:10.1371/journal.pone.0012500.s006 (2.97 MB TIF)

Video S1 Atrioventricular regurgitation in the zebrafish hearts treated with DMSO (top), calcineurin inhibitor, cyclosporine A, (middle) and IP$_3$R inhibitor, 2APB, (bottom).

Found at: doi:10.1371/journal.pone.0012500.s007 (0.32 MB MOV)

Acknowledgments

We are grateful to D. Srivastava for providing probes and for scientific discussion; J. Chen for comments; H. Kokubo for Tbx2 probe; T. Nagai for TEM; K. Matsuo for construction of adenoviral expression vector of constitutively active calcineurin; M. Hirose for technical assistance with Real-Time PCR, western blotting and immunohistochemistry; K. Kimura for technical assistance with pathology; K. Shimura, E. Tsutsui and M. Mitani for their assistance.

Author Contributions

Conceived and designed the experiments: KU TN KM HY. Performed the experiments: KU MA MN CY. Analyzed the data: KU MA. Contributed reagents/materials/analysis tools: SM TN KF TT KM HY. Wrote the papefr: KU KM HY. Organized and supervised the project: KM TT HY.

References

1. Berridge MJ, Bootman MD, Roderick HL (2003) Calcium signalling: dynamics, homeostasis and remodelling. Nat Rev Mol Cell Biol 4: 517–529.
2. Kockskamper J, Zima AV, Roderick HL, Pieske B, Blatter LA, et al. (2008) Emerging roles of inositol 1,4,5-trisphosphate signaling in cardiac myocytes. J Mol Cell Cardiol 45: 128–147.
3. Furuichi T, Yoshikawa S, Miyawaki A, Wada K, Maeda N, et al. (1989) Primary structure and functional expression of the inositol 1,4,5-trisphosphate-binding protein P400. Nature 342: 32–38.
4. Iwai M, Tateishi Y, Hattori M, Mizutani A, Nakamura T, et al. (2005) Molecular cloning of mouse type 2 and type 3 inositol 1,4,5-trisphosphate receptors and identification of a novel type 2 receptor splice variant. J Biol Chem 280: 10305–10317.
5. Matsumoto M, Nakagawa T, Inoue T, Nagata E, Tanaka K, et al. (1996) Ataxia and epileptic seizures in mice lacking type 1 inositol 1,4,5-trisphosphate receptor. Nature 379: 168–171.
6. Futatsugi A, Nakamura T, Yamada MK, Ebisui E, Nakamura K, et al. (2005) IP3 receptor types 2 and 3 mediate exocrine secretion underlying energy metabolism. Science 309: 2232–2234.
7. Takeshima H, Komazaki S, Hirose K, Nishi M, Noda T, et al. (1998) Embryonic lethality and abnormal cardiac myocytes in mice lacking ryanodine receptor type 2. Embo J 17: 3309–3316.
8. Hogan PG, Lewis RS, Rao A Molecular basis of calcium signaling in lymphocytes: STIM and ORAI. Annu Rev Immunol 28: 491–533.
9. Crabtree GR, Olson EN (2002) NFAT signaling: choreographing the social lives of cells. Cell 109 Suppl: S67–79.
10. Chang CP, Neilson JR, Bayle JH, Gestwicki JE, Kuo A, et al. (2004) A field of myocardial-endocardial NFAT signaling underlies heart valve morphogenesis. Cell 118: 649–663.
11. de la Pompa JL, Timmerman LA, Takimoto H, Yoshida H, Elia AJ, et al. (1998) Role of the NF-ATc transcription factor in morphogenesis of cardiac valves and septum. Nature 392: 182–186.
12. Ranger AM, Grusby MJ, Hodge MR, Gravallese EM, de la Brousse FC, et al. (1998) The transcription factor NF-ATc is essential for cardiac valve formation. Nature 392: 186–190.
13. Graef IA, Chen F, Chen L, Kuo A, Crabtree GR (2001) Signals transduced by Ca(2+)/calcineurin and NFATc3/c4 pattern the developing vasculature. Cell 105: 863–875.
14. Bushdid PB, Osinska H, Waclaw RR, Molkentin JD, Yutzey KE (2003) NFATc3 and NFATc4 are required for cardiac development and mitochondrial function. Circ Res 92: 1305–1313.
15. Rosemblit N, Moschella MC, Ondriasa E, Gutstein DE, Ondrias K, et al. (1999) Intracellular calcium release channel expression during embryogenesis. Dev Biol 206: 163–177.
16. Lyons GE, Schiaffino S, Sassoon D, Barton P, Buckingham M (1990) Developmental regulation of myosin gene expression in mouse cardiac muscle. J Cell Biol 111: 2427–2436.
17. Kubalak SW, Miller-Hance WC, O'Brien TX, Dyson E, Chien KR (1994) Chamber specification of atrial myosin light chain-2 expression precedes septation during murine cardiogenesis. J Biol Chem 269: 16961–16970.
18. Yuasa S, Itabashi Y, Koshimizu U, Tanaka T, Sugimura K, et al. (2005) Transient inhibition of BMP signaling by Noggin induces cardiomyocyte differentiation of mouse embryonic stem cells. Nat Biotechnol 23: 607–611.
19. Thomas T, Yamagishi H, Overbeek PA, Olson EN, Srivastava D (1998) The bHLH factors, dHAND and eHAND, specify pulmonary and systemic cardiac ventricles independent of left-right sidedness. Dev Biol 196: 228–236.
20. Nakagawa O, Nakagawa M, Richardson JA, Olson EN, Srivastava D (1999) HRT1, HRT2, and HRT3: a new subclass of bHLH transcription factors marking specific cardiac, somitic, and pharyngeal arch segments. Dev Biol 216: 72–84.
21. Copp AJ (1995) Death before birth: clues from gene knockouts and mutations. Trends Genet 11: 87–93.
22. Nakamura Y, Hamada Y, Fujiwara T, Enomoto H, Hiroe T, et al. (2005) Phospholipase C-delta1 and -delta3 are essential in the trophoblast for placental development. Mol Cell Biol 25: 10979–10988.
23. Mjaatvedt CH, Markwald RR (1989) Induction of an epithelial-mesenchymal transition by an in vivo adheron-like complex. Dev Biol 136: 118–128.

24. Maruyama T, Kanaji T, Nakade S, Kanno T, Mikoshiba K (1997) 2APB, 2-aminoethoxydiphenyl borate, a membrane-penetrable modulator of Ins(1,4,5)P3-induced Ca2+ release. J Biochem 122: 498–505.
25. O'Keefe SJ, Tamura J, Kincaid RL, Tocci MJ, O'Neill EA (1992) FK-506- and CsA-sensitive activation of the interleukin-2 promoter by calcineurin. Nature 357: 692–694.
26. Saneyoshi T, Kume S, Amasaki Y, Mikoshiba K (2002) The Wnt/calcium pathway activates NF-AT and promotes ventral cell fate in Xenopus embryos. Nature 417: 295–299.
27. Jayaraman T, Marks AR (2000) Calcineurin is downstream of the inositol 1,4,5-trisphosphate receptor in the apoptotic and cell growth pathways. J Biol Chem 275: 6417–6420.
28. Johnson EN, Lee YM, Sander TL, Rabkin E, Schoen FJ, et al. (2003) NFATc1 mediates vascular endothelial growth factor-induced proliferation of human pulmonary valve endothelial cells. J Biol Chem 278: 1686–1692.
29. Brock TA, Dvorak HF, Senger DR (1991) Tumor-secreted vascular permeability factor increases cytosolic Ca2+ and von Willebrand factor release in human endothelial cells. Am J Pathol 138: 213–221.
30. Zhou B, Cron RQ, Wu B, Genin A, Wang Z, et al. (2002) Regulation of the murine Nfatc1 gene by NFATc2. J Biol Chem 277: 10704–10711.
31. Oka T, Dai YS, Molkentin JD (2005) Regulation of calcineurin through transcriptional induction of the calcineurin A beta promoter in vitro and in vivo. Mol Cell Biol 25: 6649–6659.
32. Graef IA, Mermelstein PG, Stankunas K, Neilson JR, Deisseroth K, et al. (1999) L-type calcium channels and GSK-3 regulate the activity of NF-ATc4 in hippocampal neurons. Nature 401: 703–708.
33. Bootman MD, Collins TJ, Mackenzie L, Roderick HL, Berridge MJ, et al. (2002) 2-aminoethoxydiphenyl borate (2-APB) is a reliable blocker of store-operated Ca2+ entry but an inconsistent inhibitor of InsP3-induced Ca2+ release. Faseb J 16: 1145–1150.
34. Arron JR, Winslow MM, Polleri A, Chang CP, Wu H, et al. (2006) NFAT dysregulation by increased dosage of DSCR1 and DYRK1A on chromosome 21. Nature 441: 595–600.
35. Maeda N, Niinobe M, Nakahira K, Mikoshiba K (1988) Purification and characterization of P400 protein, a glycoprotein characteristic of Purkinje cell, from mouse cerebellum. J Neurochem 51: 1724–1730.
36. Sugiyama T, Furuya A, Monkawa T, Yamamoto-Hino M, Satoh S, et al. (1994) Monoclonal antibodies distinctively recognizing the subtypes of inositol 1,4,5-trisphosphate receptor: application to the studies on inflammatory cells. FEBS Lett 354: 149–154.
37. Yamagishi H, Olson EN, Srivastava D (2000) The basic helix-loop-helix transcription factor, dHAND, is required for vascular development. J Clin Invest 105: 261–270.

Journal of Molecular and Cellular Cardiology 49 (2010) 576–586

Contents lists available at ScienceDirect

Journal of Molecular and Cellular Cardiology

journal homepage: www.elsevier.com/locate/yjmcc

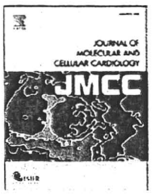

Original article

4-Hydroxy-2-nonenal protects against cardiac ischemia–reperfusion injury *via* the Nrf2-dependent pathway

Yan Zhang [a,1], Motoaki Sano [a,d,*], Ken Shinmura [b], Kayoko Tamaki [b], Yoshinori Katsumata [a], Tomohiro Matsuhashi [a], Shintaro Morizane [a], Hideyuki Ito [a], Takako Hishiki [c], Jin Endo [a], Heping Zhou [a], Shinsuke Yuasa [a], Ruri Kaneda [a], Makoto Suematsu [c], Keiichi Fukuda [a]

[a] *Department of Cardiology, Keio University School of Medicine, Tokyo, 160-8582, Japan*
[b] *Department of Geriatric Medicine, Keio University School of Medicine, Tokyo, 160-8582, Japan*
[c] *Department of Biochemistry and Integrative Medical Biology, Keio University School of Medicine, Tokyo, 160-8582, Japan*
[d] *Precursory Research for Embryonic Science and Technology (PRESTO), Japan Science and Technology Agency, Saitama, 332-0012, Japan*

ARTICLE INFO

Article history:
Received 25 December 2009
Received in revised form 24 April 2010
Accepted 21 May 2010
Available online 4 June 2010

Keywords:
4-Hydroxy-2-nonenal
Ischemia–reperfusion injury
Nrf2
Hormesis
Glutathione

ABSTRACT

Reactive oxygen species (ROS) attack polyunsaturated fatty acids of the membrane and trigger lipid peroxidation, which results in the generation of α,β-unsaturated aldehydes, such as 4-hydroxy-2-nonenal (4-HNE). There is compelling evidence that high concentrations of aldehydes are responsible for much of the damage elicited by cardiac ischemia–reperfusion injury, while sublethal concentrations of aldehydes stimulate stress resistance pathways, to achieve cardioprotection. We investigated the mechanism of cardioprotection mediated by 4-HNE. For cultured cardiomyocytes, 4-HNE was cytotoxic at higher concentrations (≥20 μM) but had no appreciable cytotoxicity at lower concentrations. Notably, a sublethal concentration (5 μM) of 4-HNE primed cardiomyocytes to become resistant to cytotoxic concentrations of 4-HNE. 4-HNE induced nuclear translocation of transcription factor NF-E2-related factor 2 (Nrf2), and enhanced the expression of γ-glutamylcysteine ligase (GCL) and the core subunit of the Xc^- high-affinity cystine transporter (xCT), thereby increasing 1.45-fold the intracellular GSH levels. Cardiomyocytes treated with either Nrf2-specific siRNA or the GCL inhibitor L-buthionine sulfoximine (BSO) were less tolerant to 4-HNE. Moreover, the cardioprotective effect of 4-HNE pretreatment against subsequent glucose-free anoxia followed by reoxygenation was completely abolished in these cells. Intravenous administration of 4-HNE (4 mg/kg) activated Nrf2 in the heart and increased the intramyocardial GSH content, and consequently improved the functional recovery of the left ventricle following ischemia–reperfusion in Langendorff-perfused hearts. This cardioprotective effect of 4-HNE was not observed for Nrf2-knockout mice. In summary, 4-HNE activates Nrf2-mediated gene expression and stimulates GSH biosynthesis, thereby conferring on cardiomyocytes protection against ischemia–reperfusion injury.

1. Introduction

Reactive oxygen species (ROS) originate from various sources, including the Nox family of NADPH oxidases, xanthine oxidase, and mitochondria, in which superoxide radicals are the byproducts of oxidative energy production. Superoxide radicals are dismuted by superoxide dismutase (SOD), to produce hydrogen peroxides, which in turn are degraded into water and molecular oxygen by catalase, glutathione peroxidase (Gpx), and peroxiredoxin (Prx). Hydroxyl radicals (OH•), which are the most potent ROS, are formed from hydrogen peroxides through the Fenton reaction. No endogenous enzymes exist to eliminate these radicals. The OH• attack neighboring polyunsaturated fatty acids in the cell membrane, thereby triggering lipid peroxidation, which results in the generation of lipid hydroperoxides and α,β-unsaturated aldehydes, including 4-hydroxy-2-nonenal (4-HNE). These aldehydes are highly electrophilic and react with biomolecules, such as proteins and nucleic acids, to generate various adducts [1]. By virtue of their high chemical stability, these lipid peroxidation products diffuse greater distances than their precursor ROS, so they can disseminate oxidative injury and amplify damage. Aldehydes accumulation is found in ischemic, hypertrophic, and failing hearts, as well as in the oxidation of LDL [2], atherosclerotic lesions, and the brains of patients with Alzheimer's disease [3], and therefore, have been implicated in the pathogenesis of oxidative stress-associated diseases. Pretreatment with a small molecule activator of an aldehyde-detoxifying enzyme, aldehyde dehydrogenase 2

---

[*] Corresponding author. Department of Cardiology, Keio University School of Medicine, 35 Shinanomachi Shinjuku-ku, Tokyo, 160-8582, Japan. Tel.: +81 3 5363 3874; fax: +81 3 5363 3875.
E-mail address: msano@sc.itc.keio.ac.jp (M. Sano).

[1] Present address: Department of Pharmacology, Harbin Medical University, Harbin, China.

0022-2828/$ - see front matter © 2010 Elsevier Ltd. All rights reserved.
doi:10.1016/j.yjmcc.2010.05.011

(ALDH2), reduced infarct size by 60% in a rat model of ischemia-reperfusion injury [4], which indicates that much of the damage inflicted by ischemia-reperfusion is attributable to aldehydes generated in the ischemic heart.

Although the pathogenic effects of ROS are well established, antioxidant supplements for the prevention of cardiovascular events have been found to lack efficacy, and may even be harmful [5]. This discrepancy may be attributable to the dual role of ROS. ROS are not simply toxic byproducts, since they also play important roles in establishing antioxidant defense mechanisms. The sensing of aldehyde accumulation in injured tissues enables the cell to activate a variety of stress resistance pathways in a cell-type-specific manner, so as to counteract oxidative stress-mediated injury [6–8]. This induction of protective mechanisms by stressors is referred to as "stress-response hormesis" [9]. Therefore, aldehydes may be regarded as second messengers that propagate ROS-initiating favorable signaling.

In the present study, we investigated whether 4-HNE, which is one of the most abundant aldehydes produced by lipid peroxidation *in vivo*, induces stress-response hormesis in cultured cardiomyocytes and in *in vivo* hearts, and determined the underlying mechanisms.

2. Materials and methods

2.1. Animals

All animal experiments were reviewed and approved by the Institutional Animal Care and Use Committee at Keio University School of Medicine. Male C57BL/6 J mice at 10 weeks of age were obtained from CLEA Japan (Tokyo, Japan). Nrf2-knockout mice on a C57BL/6 J background were generated as previously described [10]. For comparison, Nrf2-wildtype mice (C57BL/6 J) were obtained from siblings of the Nrf2-knockout.

2.2. Cell culturing

Neonatal ventricular myocytes from 1- to 2-day-old Sprague–Dawley rats were subjected to Percoll gradient centrifugation and differential plating, to enrich for cardiac myocytes and to deplete non-myocytes [11]. Cell viability was determined using the LIVE/DEAD Viability/Cytotoxicity Assay Kit (Molecular Probes), which is based on the simultaneous determination of live and dead cells with the calcein AM and ethidium homodimer-1 probes, which are specific for intracellular esterase activity and membrane integrity, respectively. Fluorescence imaging of the cells (live cells were labeled green, whereas the nuclei of dead cells were labeled red) was performed with a fluorescence microscope (BZ-9000; Keyence).

2.3. Western blotting

Nuclear extracts were prepared as described previously [11]. The following rabbit polyclonal antibodies were used: anti-Nrf2 and anti-xCT (core subunit of the Xc^- high-affinity cystine transporter) (Santa Cruz Biotechnology); anti-HO1 (hemoxygenase-1), (Stressgen); anti-catalase and anti-Gclc (catalytic subunit of γ-glutamylcysteine ligase) (Abcam); anti-Gsta2 (glutathione-S-transferase A2) (Novus Biologicals); anti-4-HNE adduct (Calbiochem). Immunoreactive proteins were visualized using horseradish peroxidase-conjugated secondary antibodies, enhanced chemiluminescence (Amersham Biosciences), and the LAS-3000 luminoimager (Fujifilm).

2.4. Quantitative Real-Time PCR

Total RNA samples from cultured cardiomyocytes and hearts were prepared using the Trizol reagent (Invitrogen), according to manufacturer's instructions. Samples of total RNA (2 μg) were reverse-transcribed using the RNA PCR Kit (Takara Biotechnology, Japan), and the resulting cDNA was used as a PCR template. The mRNA levels were determined by Real-Time PCR with the ABI PRISM 7700 Sequence Detector (Applied Biosystems), according to the manufacturer's instructions. Predesigned gene-specific primer and probe sets (TaqMan Gene Expression Assays) were used. The 18s ribosomal RNA was amplified as an internal control. The relative gene expression level (the amount of target, normalized to the endogenous control gene) was calculated using the comparative Ct method formula: $2^{-\Delta\Delta Ct}$.

2.5. siRNA oligonucleotides and transfection

The siRNA oligonucleotides directed against the rat Nrf2 and a control siRNA (Ambion) were transfected into cells using the Lipofectamine RNAiMAX reagent (Invitrogen) .

2.6. Determination of intracellular glutathione concentration

The intracellular concentration of GSH was measured spectrophotometrically (U-2810 spectrophotometer; Hitachi) using the Bioxytech GSH/GSSG-412 kit (Oxis Research), according to the manufacturer's instructions. All assays were performed in triplicate on at least three separate occasions.

2.7. Langendorff perfusion of the heart

Hearts were excised rapidly from heparinized mice, perfused with modified Krebs–Henseleit buffer (120 mmol/L NaCl, 25 mmol/L $NaHCO_3$, 5.9 mmol/L KCl, 1.2 mmol/L $MgSO_4$, 1.75 mmol/L $CaCl_2$, and 10 mmol/L glucose), and gassed with 95% O_2 and 5% CO_2 at 37 °C according to the Langendorff procedure. Coronary perfusion pressure was maintained at 90 mm Hg. A plastic catheter with a polyethylene balloon was inserted into the left ventricle (LV) through the left atrium. Before the induction of ischemia, the left ventricular end-diastolic pressure was adjusted to 10 mm Hg by filling the balloon with water. The indices of LV function, including LV systolic pressure (LVSP), LV end-diastolic pressure (LVEDP), and positive dP/dt, were recorded as described previously. The total lactate dehydrogenase (LDH) activity released into the perfusate was measured with a commercially available kit (Sigma) [11]. To examine the effect of 4-HNE treatment on function recovery after ischemia–reperfusion, mice were injected with either 4 mg/kg 4-HNE or vehicle (50 μl of saline) *via* the retro-orbital vein [12] [13]. The efficacy of injection via the retro-orbital vein was confirmed using Evans Blue (Supplemental Fig. 1).

2.8. Statistical analysis

The values are presented as mean ± SEM. Statistical significance was evaluated using 2-tailed, unpaired Student's *t*-tests for comparisons of two mean values. Multiple comparisons involving more than three groups were performed using ANOVA. A *P*-value less than 0.05 was considered statistically significant.

3. Results

3.1. High-dosage 4-HNE causes cardiomyocyte cell death

Neonatal rat cardiomyocytes were treated with various concentrations of 4-HNE for 24 h, and 4-HNE-induced cardiomyocyte toxicity was monitored (Fig. 1A, B). The viabilities of the cardiomyocytes in the presence of 0, 5, 10, 20, and 40 μM 4-HNE were 82.17% ± 3.19%, 80.96% ± 2.76%, 72.85% ± 2.06%, 28.95% ± 3.54%, and 0.00%, respectively (Fig. 1A). At concentrations >20 μM, HNE significantly decreased cell viability, whereas 5 μM or 10 μM 4-HNE showed no appreciable cytotoxicity. Based on these observations, concentrations of 4-HNE < 10 μM were selected for subsequent studies on the potential favorable effects of 4-HNE.

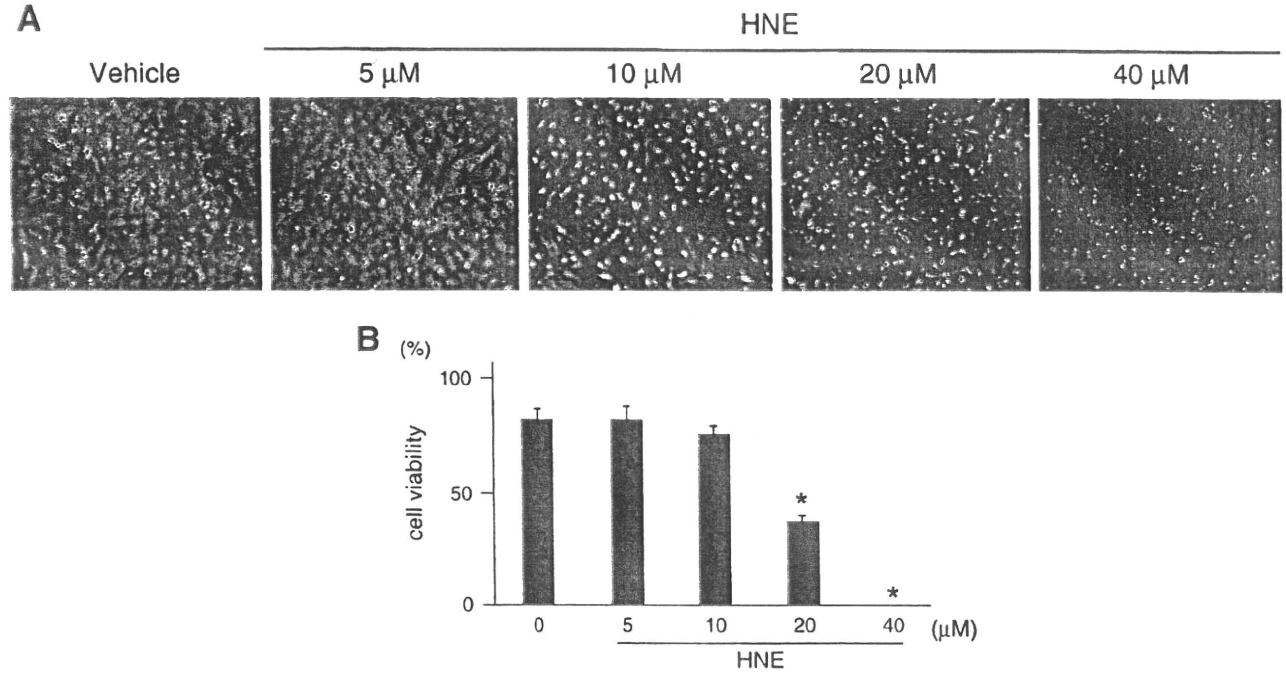

Fig. 1. 4-HNE causes cell death at higher concentrations but lacks cytotoxicity at lower concentrations. (A) Representative images of cardiomyocytes that were treated with different concentrations of 4-HNE. (B) Quantification of cell viability. Data shown are mean ± SEM ($n = 5$). $^*P<0.05$ vs. vehicle-treated cardiomyocytes (unpaired Student's t-test).

3.2. Pretreatment with a sublethal concentration of 4-HNE protects cardiomyocytes against subsequent oxidative cell death induced by a high dosage of 4-HNE

To examine the effects of 4-HNE, cardiomyocytes were pretreated with either vehicle or 5 μM 4-HNE for 14 h, and then treated with cytotoxic concentrations of 4-HNE for 24 h. The viabilities of the vehicle-pretreated cardiomyocytes were 24.59% ± 4.31% for 20 μM 4-HNE and 15.42% ± 1.76% for 30 μM 4-HNE. Pretreatment with 5 μM 4-HNE significantly increased the cardiomyocyte viabilities to 72.09% ± 5.53% for 20 μM 4-HNE and 38.65% ± 4.12% for 30 μM 4-HNE (Fig. 2A, B).

3.3. 4-HNE induces antioxidant enzymes and GSH synthesis in cardiomyocytes

We examined the underlying molecular mechanisms responsible for the cytoprotective effect of 4-HNE on cardiomyocytes. 4-HNE treatment increased both the mRNA and protein expression levels of various antioxidant enzymes, including HO-1, catalase, Gsta2, Gclc, and xCT (Fig. 3A, B). The rate of glutathione (GSH) synthesis is determined primarily by Gclc activity and the availability of precursor amino acids, especially cysteine. Consistent with the increased levels of Gclc and xCT, the intracellular concentration of GSH was increased 1.45-fold in cardiomyocytes that were treated with 5 μM 4-HNE for 24 h, as compared to cells that were treated with vehicle (261.08 ± 19.35 μM/g vs. 179.89 ± 11.59 μM/g, respectively) (Fig. 3C).

3.4. Nrf2 plays a key role in the induction of stress responses

Nrf2 has been implicated as a key transcription factor that induces the expression of antioxidant genes. Under non-stress conditions, Nrf2 is bound to Kelch-like ECH-associated protein 1 (Keap1) in the cytoplasm. This complex directs Nrf2 polyubiquitination and degradation. During oxidative stress, Nrf2 is liberated from Keap1 and enters the nucleus, where it can form a heterodimer with the small Maf transcription factor Nrf2, to stimulate the expression of antioxidant response element (ARE)-containing genes [14]. Therefore, we investigated the possibility that Nrf2 accumulates in the nucleus after 4-HNE treatment. Cultured cardiomyocytes were treated with 4-HNE for 1 h, and nuclear extracts of these cells were subjected to immunoblotting. Nuclear accumulation of Nrf2 in response to 4-HNE treatment was observed (Fig. 4A).

To investigate whether Nrf2 signaling is important for the favorable response to 4-HNE, the cardiomyocytes were subjected to RNA interference to block Nrf2 expression and then stimulated with 4-HNE (5 μM) or vehicle for 6 h. Nrf2 silencing almost completely suppressed the 4-HNE-mediated increases in the expression levels of Gclc, xCT, and Gsta2. In contrast, Nrf2 silencing only modestly suppressed the 4-HNE-mediated increase in HO-1 expression (Fig. 4B). Therefore, we examined the possible involvement of Nrf2 in the observed increased in GSH level. Nrf2 silencing cells and control cells were treated with 4-HNE (5 μM) or vehicle for 14 h. Nrf2 silencing resulted in no appreciable cytotoxicity under these conditions (data not shown). The 4-HNE-mediated increase in GSH level was markedly suppressed in Nrf2 siRNA-treated cardiomyocytes, as compared to control siRNA-treated cardiomyocytes (115.98 ± 8.63 μM/mg vs. 213.43 ± 16.24 μM/mg, respectively) (Fig. 4C).

Next, we examined the effect of Nrf2 silencing on cardiomyocyte viabilities. Cardiomyocytes were treated with either Nrf2-specific siRNA or a control siRNA for 24 h, and then stimulated with 4-HNE (5 μM or 10 μM) for 24 h. Whereas neither 5 μM nor 10 μM 4-HNE was toxic for cardiomyocytes treated with the control siRNA (81.89% ± 2.95% for 5 μM 4-HNE; 71.97% ± 4.44% for 10 μM 4-HNE), Nrf2 silencing significantly decreased cardiomyocyte viability in the presence of 4-HNE (48.94% ± 3.30% for 5 μM 4-HNE; and 14.49% ± 1.40% for 10 μM 4-HNE) (Fig. 5A, B).

To examine the role of Nrf2 in the induction of protection mediated by 4-HNE, Nrf2-depleted cardiomyocytes were preincubated with 5 μM 4-HNE for 14 h, and then stimulated with 10 μM or 20 μM of 4-HNE for an additional 24 h. Preincubation with 5 μM 4-HNE for 14 h had no appreciable cytotoxic effect on either the Nrf2-wildtype or Nrf2-depleted cardiomyocytes. However, the viabilities of

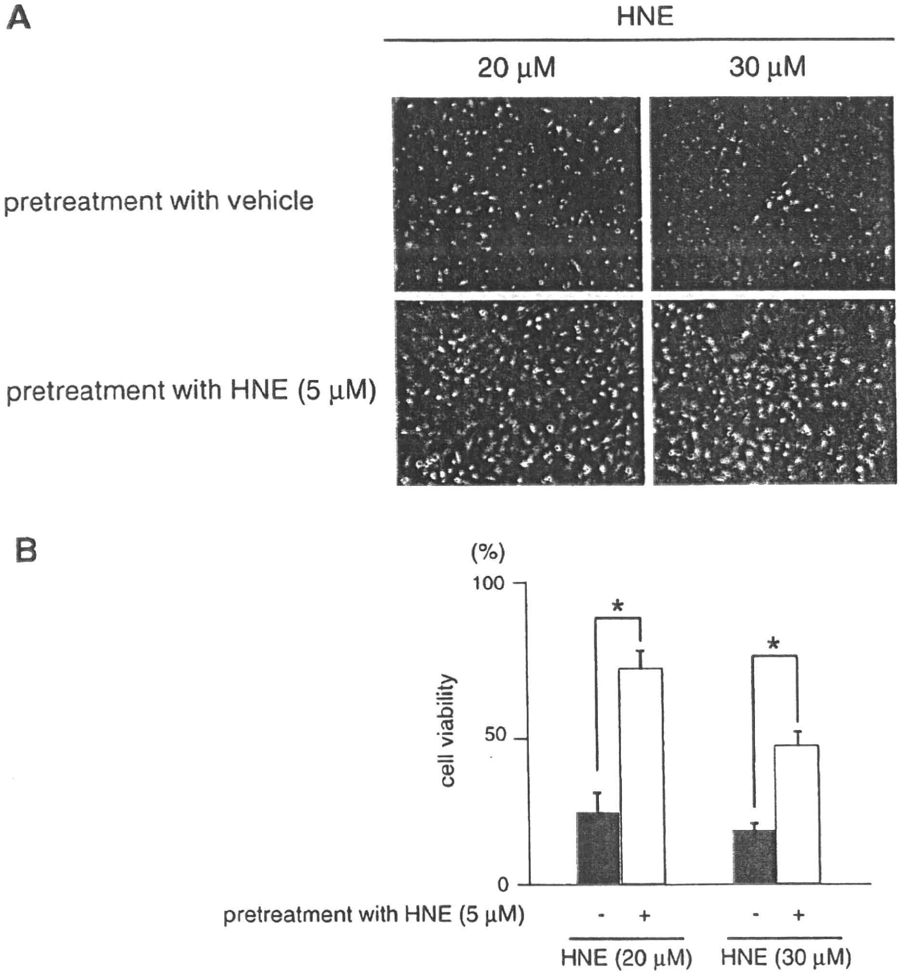

Fig. 2. Exposure to a sublethal concentration of 4-HNE enables cardiomyocytes to adapt to cytotoxic concentrations of 4-HNE. Cardiomyocytes were treated with either vehicle or 4-HNE (5 μM) for 14 h, and then incubated with a toxic concentration (20 μM or 30 μM) of 4-HNE for 24 h. (A) Representative images of cardiomyocytes that were treated with toxic concentrations of 4-HNE. (B) Quantification of cell viability. Data shown are mean ± SEM ($n = 5$). $^*P<0.05$ vs. vehicle-pretreated cardiomyocytes (unpaired Student's *t*-test).

the Nrf2-depleted cardiomyocytes in 10 μM 4-HNE and 20 μM 4-HNE were 0.00% and 0.00%, respectively, while those of the control cells were 86.69% ± 3.49% and 71.18% ± 3.43%, respectively (Fig. 5C, D).

3.5. *BSO treatment sensitizes cardiomyocytes to 4-HNE-induced cell death*

To investigate whether GSH is an important factor in tolerance to 4-HNE, cardiomyocytes were incubated with 50 μM BSO, an inhibitor of GSH biosynthesis, in the presence or absence of 4-HNE (5 μM) for 14 h. BSO treatment decreased the intracellular GSH concentration from 162.47 ± 3.02 μM/mg (vehicle-treated cardiomyocytes) to 98.98 ± 12.13 μM/mg (BSO-treated cardiomyocytes). In addition, simultaneous 4-HNE treatment (5 μM) failed to increase the intracellular GSH levels of the BSO-treated cardiomyocytes (Fig. 6A). This concentration of BSO showed no appreciable effect on cardiomyocyte viability in the absence of 4-HNE, whereas it sensitized the cardiomyocytes to 4-HNE-induced death, as compared to the vehicle treatment. The viabilities of the vehicle-pretreated cardiomyocytes were 82.64% ± 3.07% for 5 μM 4-HNE and 72.61% ± 2.02% for 10 μM 4-HNE. Pretreatment with BSO significantly decreased the cardiomyocyte viabilities to 53.60 ± 2.79% for 5 μM 4-HNE and 35.16% ± 2.40% for 10 μM 4-HNE (Fig. 6B, C).

To examine the role of GSH biosynthesis in the induction of 4-HNE-mediated protection, cardiomyocytes were incubated with 5 μM 4-HNE in the presence of 50 μM BSO for 14 h, and then stimulated with 10 μM or 20 μM 4-HNE for an additional 24 h. The preincubation with 5 μM 4-HNE for 14 h had no appreciable cytotoxicity even in the presence of 50 μM BSO. However, the cardiomyocyte viabilities for treatment with 10 μM 4-HNE and 20 μM 4-HNE were 5.88% ± 0.46% and 0.00%, respectively, in the BSO-treated groups, and 88.52% ± 1.39% and 73.77% ± 1.60%, respectively, in the control groups (Fig. 6D, E).

3.6. *4-HNE pretreatment improves the functional recovery of Langendorff-perfused hearts after ischemia–reperfusion injury*

The effect of 4-HNE treatment on function recovery after ischemia–reperfusion was studied in Langendorff-perfused mouse hearts. Mice were injected with either 4 mg/kg 4-HNE or vehicle (50 μl of saline) *via* the retro-orbital vein [12] [13], and 24 h later, the hearts were isolated and subjected to 25 min of total global ischemia, followed by 60 min of aerobic reperfusion. We selected 4 mg/kg 4-HNE as the optimal dosage based on a pilot study in which various amounts of 4-HNE were administered *via* the retro-orbital vein. We confirmed that sufficient reactive 4-HNE reaches the heart upon systemic administration within

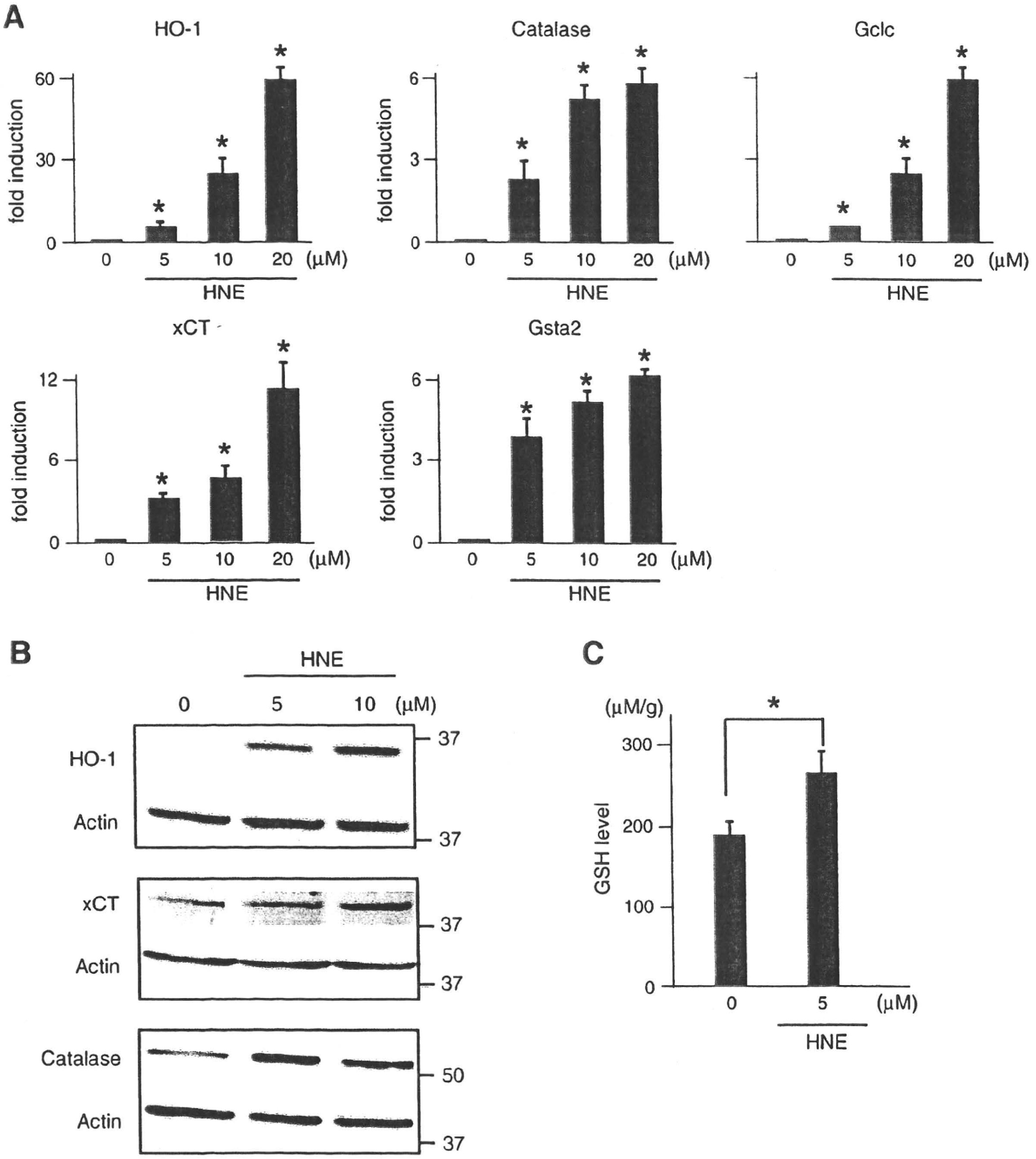

Fig. 3. 4-HNE increases the cardiomyocyte expression levels of antioxidant enzymes and GSH. (A) Cardiomyocytes were treated with different concentrations of 4-HNE (0, 5, 10, 20 μM) for 6 h. Antioxidant gene expression was determined by Q-PCR analysis. $n=5$; *$P<0.05$ vs. vehicle-treated cardiomyocytes. (B) Cardiomyocytes were treated with different concentrations of 4-HNE (0, 5, 10 μM) for 14 h. The antioxidant enzyme expression levels were determined by immunoblotting. (C) Cardiomyocytes were treated with 4-HNE for 24 h. The intracellular levels of GSH were measured using Bioxytech GSH/GSSG-412 (Oxis Research), based on the Tietze method; $n=5$, *$P<0.05$, compared to the vehicle-treated cardiomyocytes.

60 min (Supplemental Fig. 2) and activated Nrf2 in the hearts (Supplemental Fig. 3A). The administration of 4-HNE *via* the retro-orbital vein significantly upregulated the levels of mRNA for antioxidant enzymes (Supplemental Fig. 3B) and increased the GSH levels, as compared to vehicle-treated control hearts (237.41 ± 12.24 mM/g for the 4-HNE-treated group vs. 214.26 ± 4.89 mM/g for the control group; $n=4$, $P<0.05$).

4-HNE pretreatment did not affect the cardiac parameters at baseline (data not shown), whereas it significantly improved the recovery of LVDP, positive dP/dt, and negative dP/dt, as compared to the control treatment (Fig. 7). Consistent with these findings, the level of total LDH release into the perfusate during reperfusion was significantly lower in the 4-HNE-pretreatment hearts than in the control hearts.

Next, we examined the changes in the levels of 4-HNE in the hearts using antibodies specific for 4-HNE adduct proteins. Despite the significant changes in cardiac gene expression and GSH content, we did not detect any difference in the levels of 4-HNE adduct proteins between the vehicle-treated and 4-HNE-treated hearts. Ischemia-reperfusion significantly increased the levels of 4-HNE adduct proteins in the Langendorff-perfused hearts. Consistent with the significant reduction